Numerical Simulation of Complex Hydraulic Fracture Development by Coupling Geo-mechanical and Reservoir Simulator

by

Yu Wang

A thesis submitted in conformity with the requirements
for the degree of Master of Applied Science

Graduate Department of Civil and Mineral Engineering
University of Toronto

Numerical Simulation of Hydraulic Fracturing by Coupling Geo-mechanical and Reservoir Simulator

Yu Wang

Master of Applied Science

Graduate Department of Civil and Mineral Engineering
University of Toronto

2020

Abstract

Hydraulic fracturing is one of the standard techniques adopted by oil and gas industries to enhance production in unconventional reservoirs. Reservoir properties and treatment designs have a significant influence on the effectiveness of hydraulic fracturing treatments. Extensive studies on the mechanism of hydraulic fracturing have been conducted to optimize the hydraulic fracturing design. Recent advances in fracture diagnostic technology have brought new insights to the complex fracture geometry. Numerical simulation is an economical approach to investigate the generation of fracture geometry and its effect on post-treatment production enhancement. This work proposes a workflow to study the fracture complexity through coupling the geomechanical simulator Irazu and the reservoir simulator CMG. The geo-mechanical simulator is devised to simulate the hydraulic fracturing process employing the hybrid finite-discrete element method while the reservoir simulator CMG is used for the reservoir post-treatment production forecast.

Acknowledgments

I would like to express my sincerest gratitude to my mentor Prof. Giovanni Grasselli. Your dedication and enthusiasm to research have motivated me to pursue a higher standard. Thank you for providing me this precious research opportunity and sharing your expertise and guidance when I was lost and doubting myself. Without you this work would not have been possible.

I would like to thank Prof. Doug Schmitt. You impressed me with your passion on rock physics and led me into the research world that is full of excitement.

Gratitude extends to past and current members of the Geomechanics group who have provided me academic and emotional support over the years. Your enthusiasm and positive attitudes towards research always lit up the lab. I am especially grateful to Qi Zhao for his expertise on FDEM, Johnson Ha for his sense of humor and providing the FDEM simulations, Aly Abdelaziz for his “obsession” to details and optimistic spirits, Earl Magsipoc for his insights on the permeability tensor calculation, and Yusheng Qiu for suggestions on the applications of this work to field development. I will always remember the laughs we had and I hope our paths would cross again in the future.

I would like to thank prof. Karl Peterson and my committee members Prof. Giovanni Grasselli and Prof. Sebastian Goodfellow for the valuable insights and suggestions to this work.

I would like to thank my friends for always being there and providing me continual encouragement and help when I was struggling. Special thanks to my family for developing my sense of curiosity towards the world and providing support with my decisions. Your unconditional love and encouragement kept me going through tough times.

Table of Contents

List of Tables

List of Figures

Chapter 1
Introduction

1.1. Background

With the increasing interest in developing low permeability reservoirs such as tight sand or shale, various well stimulation treatments have been experimented to enhance production. As a massive amount of horizontal wells being drilled over recent years, hydraulic fracturing technology has gained the most attention in the industry (Britt & Smith, 2009; Cramer, 2008; Warpinski et al., 2009). Extensive studies have been conducted through laboratory and field experiments as well as computer modeling to understand the mechanism of hydraulic fracturing in order to provide valuable guidance on the treatment design.

Conventionally, for the purpose of studying the mechanism of hydraulic fracturing, the geometry of the fracture in rock mass has been assumed symmetric, planar, and bi-wing (Adachi et al., 2007). This simplification applies to most tight gas sand reservoirs and helped with the early rapid development of the HF technology. However, emerging evidence from fracture mapping technologies (such as microseismic and tiltmeter mapping) has shown that for most shale gas reservoirs the fracture geometry is in fact quite complex due to several factors including low stress contrast, low viscosity fracturing fluid, and pre-existing rock discontinuities (Fisher et al., 2002, 2004; Warpinski et al., 2005). This complex fracture geometry tends to have long and wide fracture "fairways", creating large surface areas in the formation such as that shown in Figure 1-1.

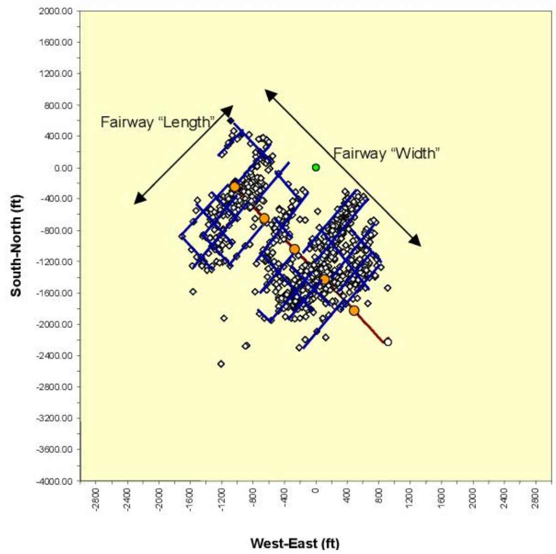

Figure 1-1 Plan view fracture mapping data of typical uncemented Barnett shale treatment with complex fracture structure illustrated using fairway "length" and "width" (Fisher et al., 2004).

To account for these new discoveries, complex fracture geometry has been incorporated into models, as illustrated in Figure 1-2.

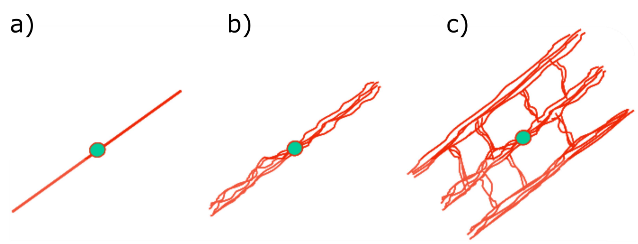

Figure 1-2 Simple to extremely complex fracture geometry. a) simple fracture; b) complex fracture; c) extremely complex fracture observed in shale gas formation after HF treatments (Fisher et al., 2004).

Conventional industry practices often correlate the success of hydraulic fracturing to total fluid volume pumped or the fracture half-length based on the simple planar fracture geometry assumption. However, advanced fracture mapping technology tells a different story. The fracture mapping results not only reveal the existence of fracture geometry complexity but also provide insights on the effectiveness of hydraulic fracturing by correlating the post-treatment production enhancement with fracture complexity. Field results suggest that the EUR (estimated ultimate recovery) is correlated to the complexity of the fracture network as opposed to the fracture half-length as conventionally interpreted in the simple bi-wing planar fracture geometry (Fan et al., 2010; Fisher et al., 2004). In light of this discovery, unconventional reservoir developers started focusing on how to generate complex fracture geometry and what is its effect on post-treatment performance.

Although there have been continuous studies on mapping the complex fracture geometry through field diagnostic tools or through laboratory imaging techniques such as micro-CT (De Kock et al., 2015; Ramandi et al., 2016), a direct measure of the fracture geometry during hydraulic fracturing is not always economically viable. In comparison, reliable numerical simulation can serve as a more efficient solution to study the questions proposed above.

This research proposes a workflow to couple the geomechanical simulator and the reservoir simulator, which are capable of modeling the complex fracture geometry and its effect on production enhancement, respectively.

1.2. Thesis structure

This thesis is divided into five chapters, proposing a workflow to couple the geomechanical simulator and the reservoir simulator with the ultimate goal of providing support to hydraulic fracturing treatment design.

Chapter 1 provides a brief literature review on the numerical modeling of hydraulic fracturing and their limitation on studying the complex fracture geometry. The advantages of using the hybrid finite-discrete element modeling (FDEM) technique over the previously developed methods are stated.

Chapter 2 further demonstrates the capability of FDEM to simulate the hydraulic fracturing process and provides interpretations of the complex induced fracture geometry in terms of the local permeability tensor.

Comparisons are made for these models and similar parameters used in the reservoir simulator CMG IMEX in Chapter 3.

Chapter 4 provides an example explaining the detailed workflow to couple the two simulators.

The above discussions are summarized in Chapter 5 with future research directions proposed.

1.3. Hydraulic fracturing models

1.3.1. Analytical models

With a successful numerical simulation of the treatment, its result would provide valuable guidance on the treatment design and long-term performance forecasting. This section provides a brief review of the history of numerical simulation techniques used for hydraulic fracturing.

Initially, there is no modeling involved in the treatment design in industry practice in the early 1930s. The fracturing fluid is just pumped with slurry to "open" the formation as production enhancement was profitable enough via this kind of simple treatments. The need to use modeling to aid with treatment design was not significant until about a decade later, when significant premature "screen-outs" of proppants have been seen in the treatments causing economic loss (Adachi et al., 2007). To minimize the economic loss, simple 2-D fracture models were utilized in the treatment design calculations, as described below.

KGD model (Geertsma J; & F, 1969; Khristianovic & Zheltov, 1955) assumes plane strain condition for fracture in the horizontal plane. The fracture height is pre-determined and fixed while the fracture width is constant along the vertical direction as illustrated in Figure 1-3. This model advances in analyzing fracture geometry in "open-hole" stress state where the fractures are typically short, with the length-to-height ratio smaller than one so that the fixed-width approximation can be deemed valid.

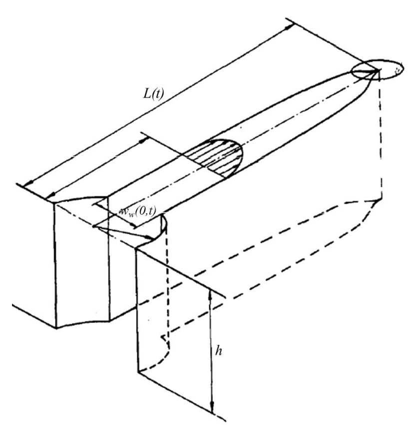

Figure 1-3 KGD model of fracture geometry (Wu, 2014).

PKN model (Nordgren, 1972; Perkins & Kern, 1961) assumes plane strain for a fracture in the vertical plane as in Figure 1-4. Same as KGD model, this model also assumes fixed fracture height while fracture width varies at different fracture height, with an elliptical vertical fracture cross-section, making it suitable for modeling fractures which are long with limited height.

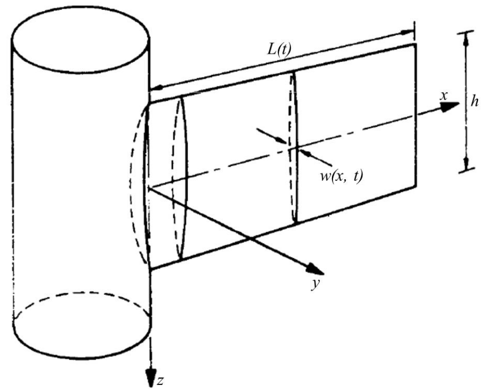

Figure 1-4 PKN model of fracture geometry with a vertical wellbore (Wu, 2014).

Abe (1976) solves for a penny-shaped, or radial-shaped crack propagation criterion under plane strain condition based on the elasticity theory proposed by Sneddon (1946). The model assumes constant loading (fluid pressure or far-field stress) throughout the fracture, applicable for the homogeneous reservoir which can be considered infinite compared to the size of the fracture.

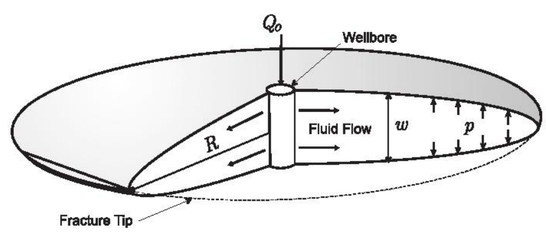

Figure 1-5 Penny-shaped radial fracture geometry (Adachi et al., 2007).

As it became more profitable to massively develop the low permeability reservoirs with the increasing oil price in the late 1970s, hydraulic treatments started targeting larger reservoir volumes across layers. Models with the incorporation of discretized fracture geometry emerged with the need to account for varying rock properties across the large stimulation zone. Pseudo-3D models allow for variation of fracture length and width at different height of the fracturing, as it accounts for the heterogeneity in different layers of the rock (Figure 1-6) (Advani & Lee, 1982; Fung et al., 1987; Settari & Cleary, 1986; Simonson et al., 1978).

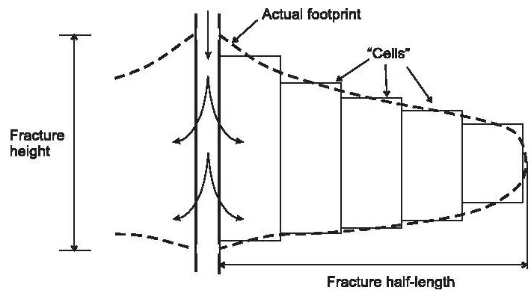

Figure 1-6 Pseudo 3D fracture geometry (Adachi et al., 2007).

Planar-3D models developed from 1980 to 2000 (Advani et al., 1990; Siebrits & Peirce, 2002) allow the rock property values in question to vary on a discretized 2-D geometry to calculate the crack aperture change as a response to the fluid pressure. Numerical solvers are used to compute the deformation on the rock mass as a continuum surrounding the fracture. However, the direction of the fracture growth is still restricted to one specific plane perpendicular to the minimum principal stress σ_3.

Giving the need to calculate 3-D fracture geometry, fully 3-D models (Lam et al., 1986; Sousa et al., 1993; Vandamme & Curran, 1989) were introduced, accounting for the heterogeneity and anisotropy of the rock mechanical properties.

The analytical models above can calculate the geometry of the fracture generated as a response to different hydraulic loading conditions. This calculation plays an important role as a measure to directly provide estimates for the critical operation parameters needed to achieve the desired fracture penetration (Adachi et al., 2007).

However, if the physical processes involved in hydraulic fracturing are taken under closer examination, there are limitations by making the respective assumptions and simplifications in the above models. There are three main stages of physical processes that need to be described during the hydraulic fracturing: fracture initiation in the intact rock under the excessive hydraulic pressure, fluid flow in the fracture channel, and the fracture growth due to the fluid pressure applied on the fracture surface.

The above mathematical solutions for the fracture geometry calculations are based on a few assumptions and simplifications: rock mass is assumed linear elastic, homogenous, and isotropic. Mode II or III crack (shearing or tearing mode) are not considered for fracture mechanics. Therefore, these models are unable to simulate fracture propagation in the rock mass under complex in-situ stress where heterogeneity and anisotropy exists. The interaction between the hydraulically induced fracture and the pre-existing discontinuities in the rock mass or the interaction between the hydraulic fracture—which are proven substantial in both laboratory testing and field monitoring (Dahi-Taleghani & Olson, 2011; Warpinski & Teufel, 1987)—could not be captured.

1.3.2 Continuum and discontinuum numerical models

As a natural next step on the evolution of numerically simulating hydraulic fracturing, partially discretized models are proposed to reduce the assumptions and simplifications made for the models introduced above. By directly incorporating a fluid solver in a DFN (discrete fracture network) and then coupling with the surrounding elastic rock continuum, these models can better describe the heterogeneity and anisotropy nature of the rock mass (Dershowitz et al., 2010; Du et al., 2010; Rogers et al., 2011). However, these models lack the capacity to simulate the new fractures generated on or propagate to the surrounding elastic rock mass. Consequently, these models cannot capture the interaction between the fractures. To overcome this limitation, fully discretized models are proposed to couple with the fluid solver. These models can be divided into continuum and discontinuum modeling techniques as introduced below.

The continuum-based modeling approaches consider the entire rock mass to be a continuum body. However, when it is needed to simulate discontinuity, continuum models cannot capture the strain localization (De Borst et al., 1993).To remedy this shortcoming, re-meshing before the fracture tip combining discrete joint model is proposed to couple with finite volume method (FVM) solving for flow in the DFN (Fu et al., 2013). Methods based on extended FEM (XFEM) are proposed (Budyn et al., 2004; Chen, 2013; Dahi-Taleghani & Olson, 2011; Keshavarzi et al., 2012; Moës et al., 1999) where re-meshing is not needed and thus saving computation costs. XFEM methods also possess the advantage that the generated fracture path is independent of the mesh configuration.

When simulating hydraulic fracturing, discontinuum-based methods or discrete modeling techniques treat the rock mass as separate bodies. Among the approaches that solve the equations of motion using an explicit time domain integration scheme, PFC (Potyondy, 2012) and UDEC (Itasca, 1996) are commonly used in the industry design. PFC divides the continuum into non-deformable particles with varying diameters and contact/parallel bonding between particles. UDEC uses polygonal blocks which resembles more to the grain structure in the rock mass. Extensive reviews of discrete modeling methods have been conducted (Hattori et al., 2017; Lisjak & Grasselli, 2014).

The hybrid continuum-discontinuum technique inherits the advantage of the continuum-based methods on calculating the internal force and failure criterion implementation while adopting the ability of explicitly modeling discontinuities both pre-existing and induced during hydraulic fracturing in the rock mass.

Among the hybrid methods, the modeling technique adopted in this research uses the3-D hybrid finite-discrete element modeling (FDEM) technique (Lisjak et al., 2015; Mahabadi et al., 2012; Munjiza, 2004; Munjiza et al., 1995). The tetrahedral elements are used to discretize the initial continuum rock mass while the softening and breakage of cohesive crack elements are used to explicitly capture the fracturing process. Shearing behaviors caused by pre-existing weak planes in the rock can be simulated by incorporating Mode II and III failures calculating the opening and the slip between the tetrahedral elements (Lisjak et al., 2014). A detailed explanation of the calculation of the internal forces and the failure criterion implemented is provided in later chapters.

Chapter 2
Hydraulic fracturing simulations using Hybrid Finite-Discrete Element method

2.1. Introduction

Upon the discussion carried out in Chapter 1, a complex geometry of fluid-induced fracture is usually observed in laboratory testing through micro-CT imaging technique and also confirmed by micro-seismic data obtained in the field.

In order to better understand the hydraulic fracturing process by investigating the roles of various operating parameters during hydraulic fracturing, a realistic numerical simulation of the process is necessary. In this chapter, the simulation of hydraulic fracturing using the hybrid finite-discrete element method (FDEM) is presented, and its capacity to simulate the complex fracture geometry is demonstrated. Validation of the model is also provided by examining the geometry of the fracture generated.

In most cases, the effect of hydraulic fracturing treatment is recognized by the vast increase of the permeability of the originally tight rock mass. The calculation of the local permeability of the simulated fractured rock mass is presented.

2.2. Numerical simulation of the hydraulic fracturing process

2.2.1. Hybrid finite-discrete element method

The simulation is conducted using the FDEM, inheriting the advantage of the finite element continuum meshing while combining the advantage of the discrete element method of using the cohesive crack element to capture fracturing behavior and solid interaction. The 3-D FDEM model utilizes an unstructured tetrahedral FEM mesh to discretize the intact rock mass. The tetrahedral constant-strain finite elements based on the classic elastic continuum simulate the elastic behavior of the rock mass. Whereas the cohesive crack elements (CCE) connecting the tetrahedral elements are able to capture the yielding, plastic deformation, and the post-fracturing behavior explicitly as shown in Figure 2-1. This combination realizes a more accurate simulation of the fracturing process of the rock mass. The concept of non-linear fracture mechanics (Barenblatt, 1962; Dugdale, 1960) is utilized to capture the strain-softening process in order to better describe the fracture initiation and propagation stages, as further illustrated below.

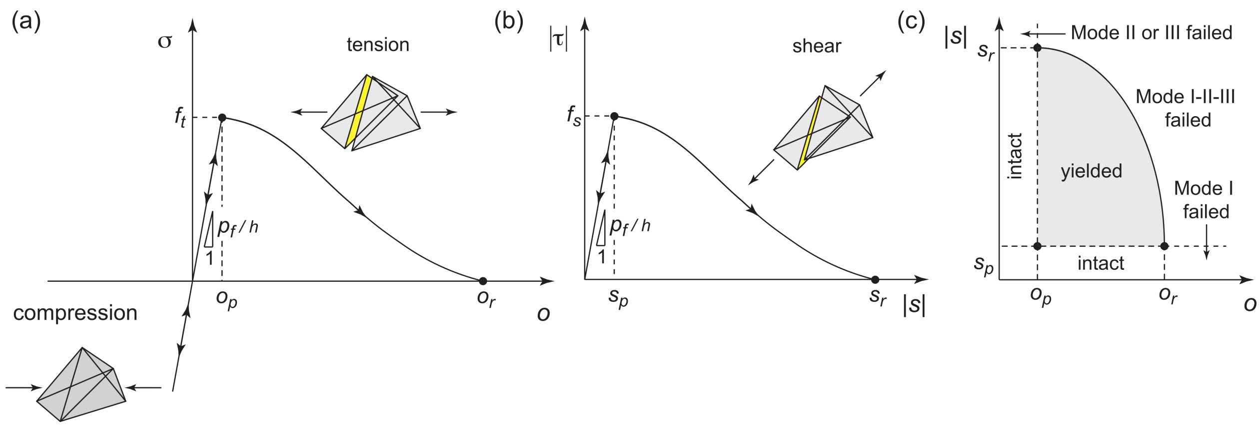

Figure 2-1 Fracture model implemented in 3-D. a) Mode I: tensile failure (opening mode); b) Mode II or III: shearing or tearing mode (out-of-plane shearing); and c) Mixed-mode failure. (Geomechanica Inc., 2018)

I) Failure mode I: opening mode

The cohesive crack element (CCE) between the constant-strain finite element pair deforms elastically until the opening O between two elements reaches critical value o_p corresponding to the tensile strength f_t on the stress-strain relationship as shown in Figure 2-1. When the normal stress acting on the CCE exceeds the critical value f_t, the opening between the two elements exceeds the critical value o_p as well, then the crack element undergoes plastic deformation governed by the energy-based constitutive relationship (Figure 2-1), the normal stress reduces as the CCE keeps yielding until it breaks where the opening of the crack element reaches the residue value o_r (Hillerborg et al., 1976; Geomechanica Inc., 2018).

II) Failure mode II or III: shearing or tearing

When the tangential bonding force is applied between the contacting element pair, it can be expressed as a function of the slip displacement and the normal stress based on a slip-weakening model (Ida, 1972). The slip s between the two elements keep increasing upon reaching a critical value s_p corresponding to the cohesive shear strength of the rock, f_s as in equation (1). While the tangential force gradually decreases as the slip reaches the maximum value s_r before the cohesive element is considered broken.

$$f_s = c + \sigma_n \cdot tan\varphi_i \tag{1}$$

Where c is the internal cohesion, φ_i is the intact material friction angle, and σ_n is the normal stress acting across the crack element.

III) Mixed failure mode

When both slipping and opening are occurring between two contacting elements, the failure of the CCE is categorized as the mixed-mode with the criterion equation (2)

$$\left(\frac{o-o_p}{o_r-o_p}\right)^2 + \left(\frac{s-s_p}{s_r-s_p}\right)^2 \geq 1 \tag{2}$$

IV) Failure mode calculation in Irazu

The failure mode, m, of a crack element is computed as follows:

$$m = \begin{cases} 1.0 & \text{if } o > o_r \ \& \ s < s_r \text{ (i.e., Mode I),} \\ 1.0 + \frac{s - s_p}{s_r - s_p} & \text{if } o < o_r \ \& \ s < s_r \text{ (with } D = 1\text{) (i.e., mixed Mode),} \\ 2.0 & \text{if } o < or \ \& \ s - s_r \text{ (i.e., Mode II or III),} \\ 3.0 & \text{if } o < o_r \ \& \ s > s_r \text{ (i.e., Mode I and II (or III)).} \end{cases}$$

(3)

Where D is a damage coefficient with a value between 0 and 1 calculated respectively for failure Mode I, II and III as follows:

$$D = \frac{o-o_p}{o_r-o_p} \tag{4}$$

$$D = \frac{s-s_p}{s_r-s_p} \tag{5}$$

$$D = \sqrt{\left(\frac{o-o_p}{o_r-o_p}\right)^2 + \left(\frac{s-s_p}{s_r-s_p}\right)^2} \tag{6}$$

V) Fracture process zone

As described above, the post-peak strain-softening behavior is captured when the cohesive elements undergo yielding before breakage, where they can still transfer load. The cohesive elements that are under plastic deformation forming an area referred to the fracture process zone at fracture tip. Broken cohesive crack elements (BCCE) are removed upon reaching the residual displacement and new fracture surfaces form (Zhao et al., 2014; Zhao, 2017). In this way, fracture initiation and propagation processes in the rock mass are explicitly captured.

The values of residual slip s_r and residual opening o_r are determined by the values of f_t, f_s, and the mode I and II fracture energies given by equation (4) and (5). The values of fracture energy are equal to the area under the curves in Figure 2-1.

$$G_{f_I} = \int_{o_p}^{o_r} \sigma(o)\, do \tag{7}$$

$$G_{f_{II-III}} = \int_{s_p}^{s_r} [\tau(s) - f_r]\, ds \tag{8}$$

VI) Reduce the influence of the crack elements on material stiffness

As introduced above, there should be zero deformation on the cohesive elements before peak strength is reached. However, the numerical model needs a finite stiffness value to run successfully. The solution is to give the crack elements a stiffness value controlled by the fracture penalty value p_f. High fracture penalty values would reduce the influence of the crack elements on the material stiffness, while higher computation time is required.

2.2.2. Coupling fluid solver to the model

In order to simulate the hydraulic fracturing process, hydraulic calculation and mechanical calculation need to be coupled in order to demonstrate the fluid flow effect on the geometry of the fracture and how the complex fracture geometry determines the fluid flow behavior in return. The below sections illustrate the process of coupling the fluid solver to the mechanical solver, incorporating the advantage of the introduction of the 6-noded cohesive crack elements into the model.

I) Flow channel

The flow channel in the 3-D FDEM model is formed by the two triangular surfaces between the two adjacent tetrahedral finite elements, as shown in Figure 2-2. Fluid flow is allowed from cavities to cavities through the connecting network connecting them (Lisjak et al., 2016). The fluid pressure is either determined by the user or calculated from the assigned flow rate. The flow rate is calculated based on Darcy's law with the assumption of parallel plate model, for example, along x-direction:

$$q_x = -\frac{\partial \bar{P}}{\partial x}\frac{a^3}{12\upsilon_f} \tag{9}$$

Where $\frac{\partial \bar{P}}{\partial x}$ is the pressure gradient along x-direction, a is the average aperture calculated as in equation (7), and υ_f is the fluid kinematic viscosity.

II) Aperture

The aperture of one fluid flow channel element can be calculated as the average of the aperture at three adjacent cavities $a_0, a_1, and\ a_2$ related to the initial aperture and the opening of the crack elements (Lisjak et al., 2016), as illustrated in equation (10). Since the opening of crack elements varies, the aperture value also differs from each flow channel:

$$a_0 = a_i + o_0 \tag{10}$$

Where a_i is the initial hydraulic aperture set by the user in the model for the rock mass, o_0 is the opening of the crack element at node 0 at this time step calculated by the mechanical solver.

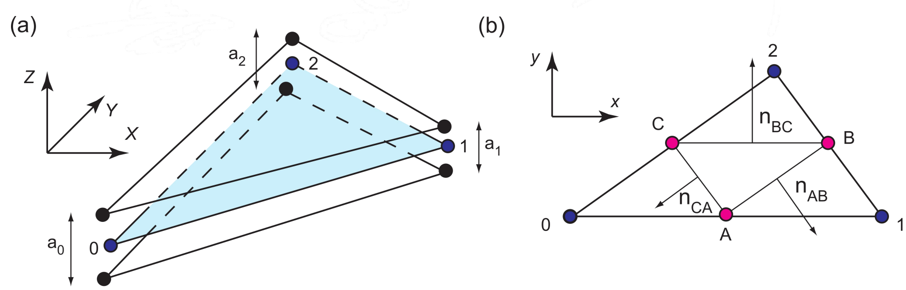

Figure 2-2 Flow channel illustration (Geomechanica Inc., 2018).

III) Coupling of hydraulic and mechanical solver

An iterative coupling regime is achieved through the following process, as illustrated in Figure 2-3. The nodal force at each cavity is calculated in the mechanical solver with the addition of the fluid pressure applied on to the surface of the flow channel. Given this updated stress field, the resulting behavior of the flow channel (cohesive crack element) is calculated in the mechanical solver based on the constitutive relationship described in Figure 2-1. The aperture of the corresponding flow channel is then updated using the calculated opening of the cohesive element, passing on to the fluid solver. The new fluid pressure can then be calculated given the compressibility of the fluid and the volume change of the fluid in the flow channel due to the aperture change.

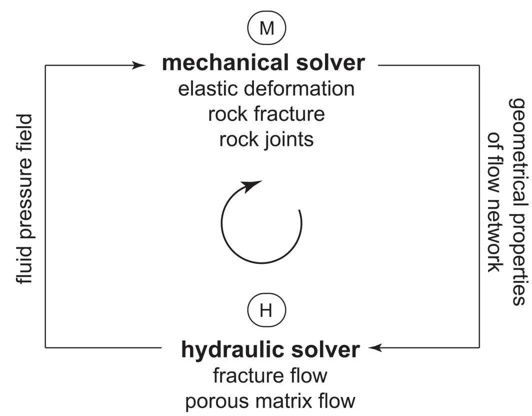

Figure 2-3 Iterative coupling regime of the mechanical and hydraulic solvers (Geomechanica Inc., 2018).

2.3. Numerical simulation example

2.3.1. Single-stage injection

The geomechanical properties for the rock mass in this hydraulic fracturing simulation example is given below in Table 2-1. Calibration process has been performed to select the optimum parameters for the microscopic mechanical properties so that the macroscopic mechanical properties of the rock modeled match the mechanical responses observed during laboratory testing (Tatone & Grasselli, 2015). The calibration process is omitted here.

A cube with a dimension of 80x80x80 mm^3 is used to simulate the reservoir rock. Fluid is injected from a cavity located at the center of the cube at a constant rate of 0.5 kg/s after the initial in-situ stress is assigned, for 10000 time steps with the time step size of $1.1*10^{-6}$ sec/time step.

Table 2-1 Geo-mechanical properties of the rock mass and cohesive crack elements.

Property (unit)	Value
Density, ρ (kg/m^3)	2500
Young's modulus, E (GPa)	30
Poisson’s ratio, ν (-)	0.2
Internal friction coefficient, μ_i (-)	0.6
Internal cohesion, c (MPa)	20
Intrinsic tensile strength, f_t (MPa)	5
Mode I fracture energy, G_{Ic} (J/m^2)	10
Mode II fracture energy, G_{IIc} (J/m^2)	100

Table 2-2 Initial stress condition for the reservoir.

Property (unit)	Value
Initial in-situ horizontal major principal stress σ_{xx} (MPa)	20
Initial in-situ horizontal minor principal stress σ_{yy} (MPa)	25
Initial in-situ vertical stress σ_{zz} (MPa)	30
Initial fluid pressure in the reservoir P_o (MPa)	0

2.4. Results and discussion

2.4.1. Fracture geometry and failure modes

The fractured zones are identified by thresholding the failure mode of the broken cohesive crack elements, and then the coordinates of these elements are exported from the visualization software *Paraview*. In the example of this single-stage hydraulic fracturing, 266 elements are identified as broken joints, as shown below in Figure 2-4, colored with failure mode calculated using equation (3) above. Most of the BCCEs failed in Mode I – tensile failure, while some BCCEs failed in mixed mode. Fracture plane is roughly perpendicular to the x-axis, although each BCCE has its unique orientation deviated from the y-z plane.

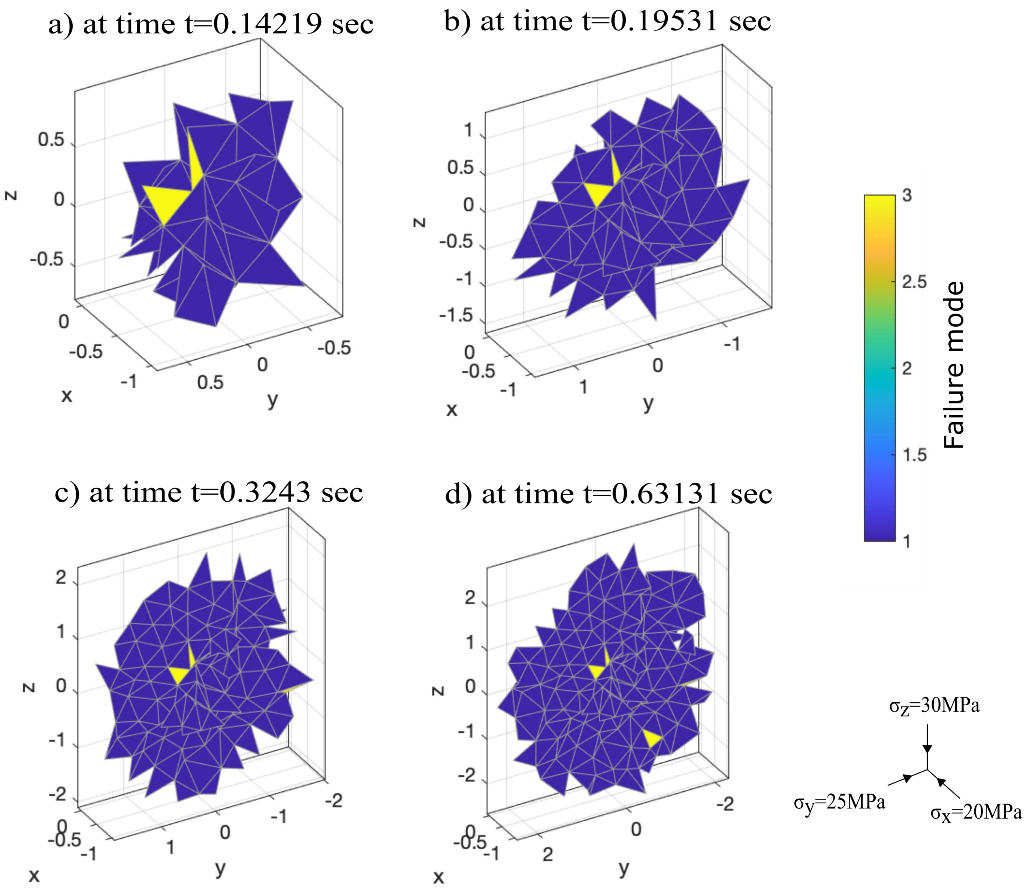

Figure 2-4 Fracture geometry and failure mode of the BCCEs at incremental time step during the fracture growth, most BCCEs fail in Mode I—tensile failure colored in dark blue, while very few fail in mixed mode colored in yellow. No pure Mode II or III—pure shearing or tearing failure is observed.

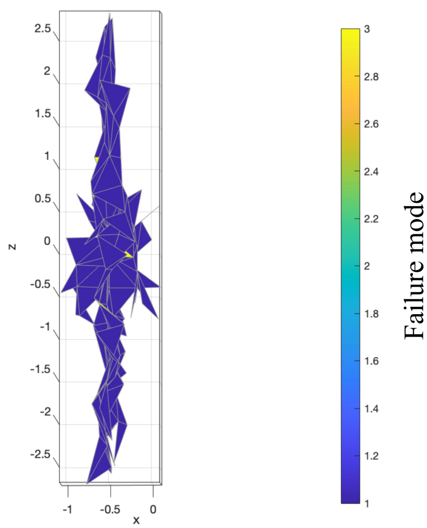

Figure 2-5 Side view of the fracture "plane".

As can be seen from the side view in Figure 2-5, there are more BCCEs at the center of the fracture plane compared to the edge. This is probably caused by the higher fluid pressure near the injection point.

2.4.2. Permeability tensor

i. Local permeability calculation

The connected flow channels (broken cohesive crack elements), which represent the fractured zone in the rock mass, can be visualized. As mentioned above, the aperture between the upper and bottom surfaces varies in every flow channel, where the resulting varying permeability can be calculated based on the "cubic law" assuming parallel plate model for single-phase fluid flow (Pyrack-Nolte et al., 1987; Reynolds, 1886; Zimmerman & Bodvarsson, 1994) derived from Navier-Stokes equations (Stokes, 1905):

$$K = \frac{a^2}{12} \tag{11}$$

However, this calculation only gives the absolute magnitude of the permeability, whereas permeability should be treated as a tensor with values at directions defined. Since the fluid is only allowed to flow through the flow channel, the magnitude calculated above determines how much fluid is allowed within the plane of the crack element. The flow perpendicular to the flow channel is restricted, which is along the normal vector to the plane of the flow channel, as illustrated in Figure 2-6. The permeability along this direction has a magnitude of zero.

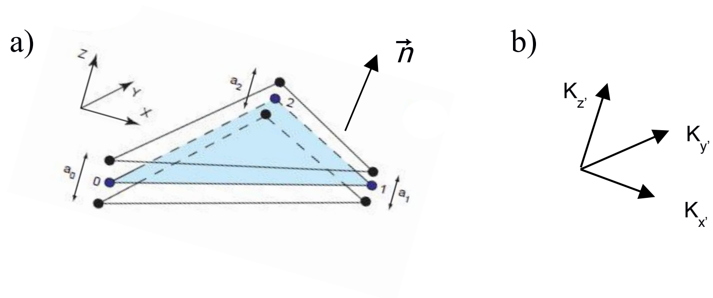

Figure 2-6 a) Direction of one crack element (flow channel) represented by its normal vector; b) Local coordinate system of the permeability tensor.

ii. Permeability tensor transformation into the global coordinate system

As can be observed from Figure 2-4 that broken crack elements (BCCE) have various orientations instead of falling in the same plane. Therefore, defining the direction of the local permeability is necessary for future fluid flow calculations in the reservoir simulator. In order to manipulate the permeability of every CCE for future reservoir fluid flow simulation in the global cartesian coordinates (x, y, and z-direction), the permeability tensor has to be defined in the global coordinates. To achieve this goal, the permeability tensor can be projected onto the global cartesian axes. For every BCCE, the following manipulation can be implemented: subtracting the component in the direction of the normal vector from the component in the direction of the base vector of that crack element as described in equation (12):

$$\vec{K} = [K_x \quad K_y \quad K_z] = K \times [1 \quad 1 \quad 1] - K \times \vec{n} \qquad (12)$$

Where $\vec{K}$ is the calculated permeability tensor for a BCCE, K is the absolute value (magnitude) of the permeability of the flow channel as calculated above in equation (11), [1 1 1] is the unit base vector which has unit magnitude in the x, y, and z-axis directions, and $\vec{n}$ is the normal vector in global coordinates, as shown on above illustration Figure 2-6.

Now permeability tensor is expressed in terms of the global coordinate system for every crack element. In this way, it can be determined how much flow is allowed in the x, y, and z-direction respectively when fluid passes through the local fracture channel.

2.4.3. Heterogeneity and anisotropy of the fracture geometry

i. Heterogeneity of the permeability tensor

The magnitude of permeability for each BCCE can be calculated using equation (12). Taking the fracture network generated in Irazu in Figure 2-4, the permeability can be mapped, as shown in Figure 2-7. It can be clearly seen that the permeability at different BCCEs (or flow channels) has different values. The relatively larger permeability in the centre of the fracture indicates a larger aperture near the injection point, which validates this model.

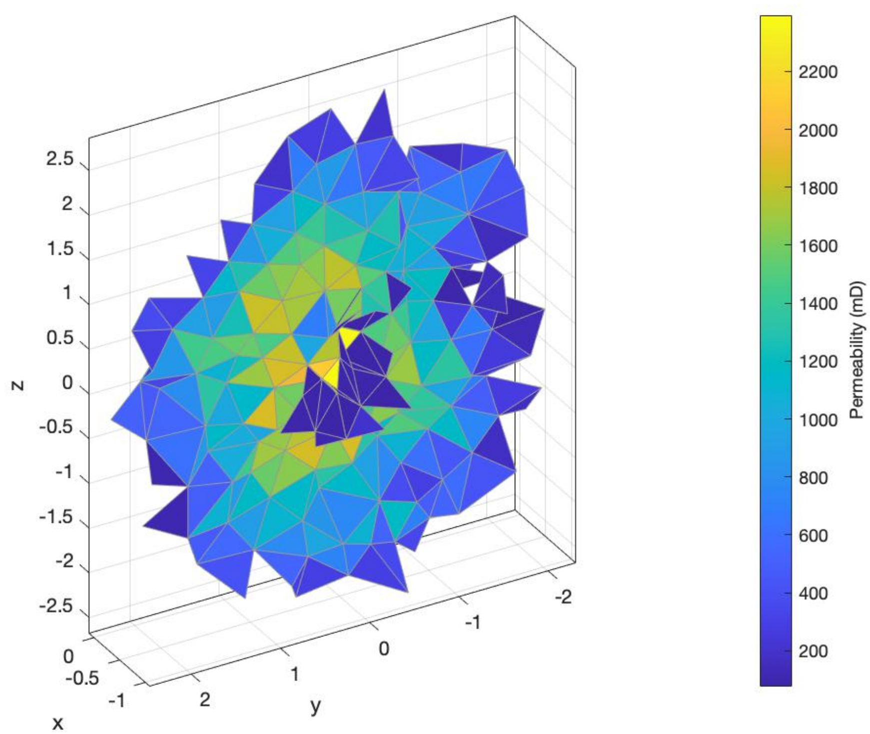

Figure 2-7 Magnitude of the total permeability at each flow channel or BCCE (broken cohesive crack element).

ii. Anisotropy of the permeability

The direction of each flow channel can be represented by its normal vector, as shown in Figure 2-8. Most of the normal vectors are along the x-axis since the fracture plane is approximately parallel to the y-z plane, as shown in Figure 2-4. For a more intuitive illustration, the angle between the normal vectors and y-axis projected on the x-z plane is calculated. The distribution of the angle is plotted in Figure 2-8 b), suggesting most BCCEs have a direction between 0 to 30 degree from the xy-z plane.

a) Normal vector plotted on each BCCE b) Dip of each BCCE from y-z plane

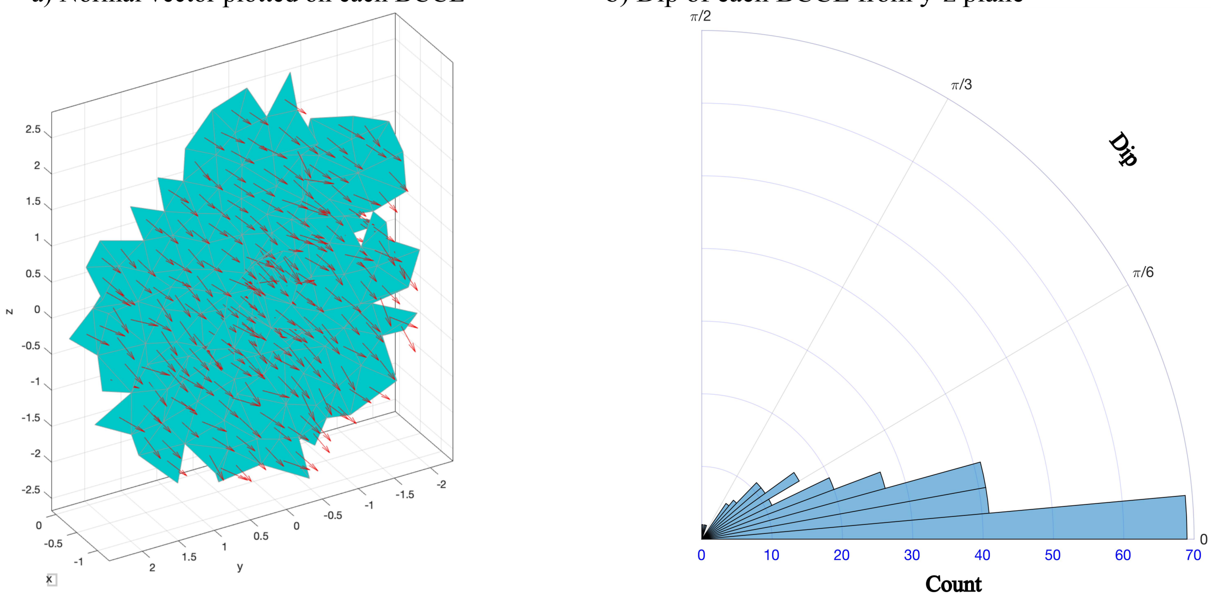

Figure 2-8 Illustration of permeability direction at each BCCE. a) normal vector (red) at each BCCE (turquoise); b) rose diagram of the angle between BCCE and y-z plane.

Since the permeability tensor can be expressed in global coordinates using equation (12), the anisotropy of the permeability tensor can be further illustrated by plotting the K_x, K_y, and K_z respectively on each BCCE as shown in Figure 2-9.

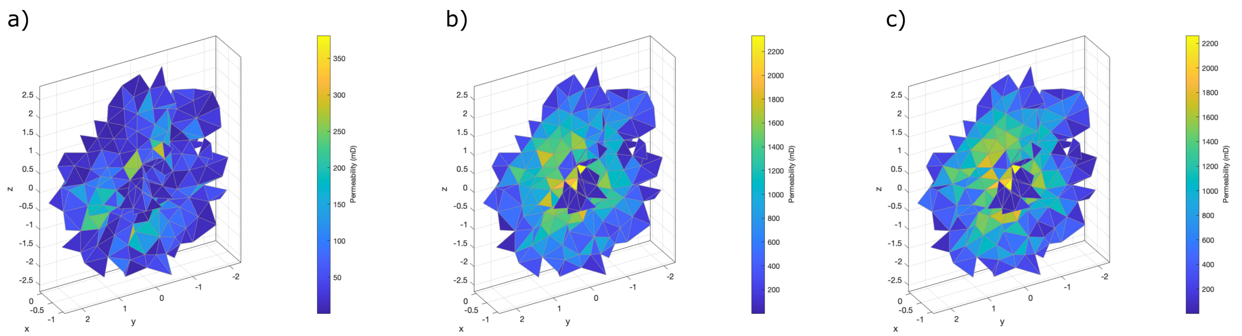

Figure 2-9 Permeability of each flow channel (BCCE) resolved to a) x-axis; b) y-axis; x) z-axis direction; i.e., K_x, K_y, and K_z.

2.5. Interactions between fracturing stages

Contrary to the intuitive belief that the more fracture is generated, the larger the SRV (stimulated reservoir volume), there exists a dilemma between fracture spacing and "stress shadow" effect. It is observed in field treatment that hydraulic fractures that are too closely spaced shed a shadow on adjacent fracture growth (Cipolla et al., 2010; Fisher et al., 2004; Nagel et al., 2013; Warpinski et al., 2009; Warpinski & Branagan, 1989). A balance between large SRV and fracture spacing (cluster spacing or stage spacing) in hydraulic fracturing design is critical to a successful treatment. The stress shadow describes the in-situ stress disturbance caused by fracture growth, as illustrated in Figure 2-10.

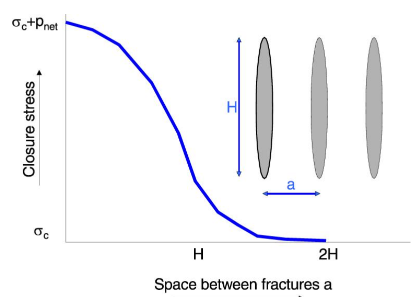

Figure 2-10 Stress disturbance of adjacent fracture growth (Fisher et al., 2004).

Two simultaneous injections were simulated in Irazu, with an identical injection rate, the fractures generated in the rock mass are illustrated in Figure 2-11. The height of the left fracture is visibly less than the fracture on the right in the side view, suggesting the inhibition effect of fracture growth by adjacent fractures.

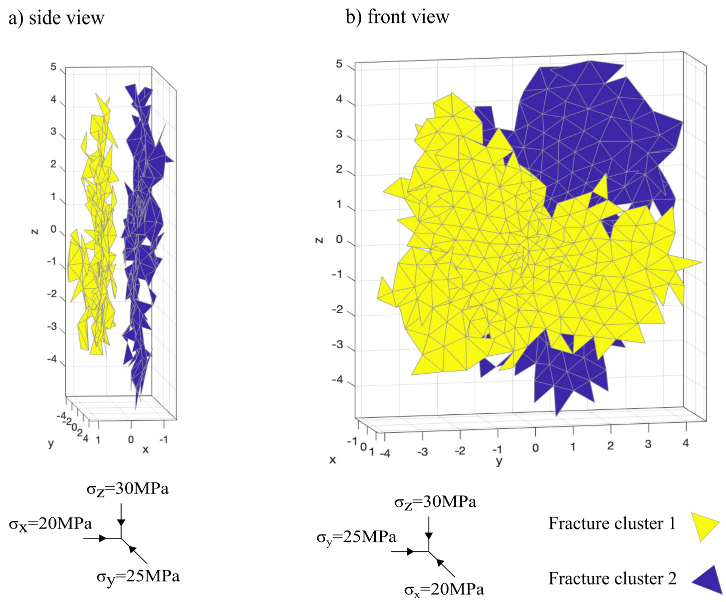

Figure 2-11 Fracture geometry of two simultaneous injections, the side-view of the fracture planes is shown here.

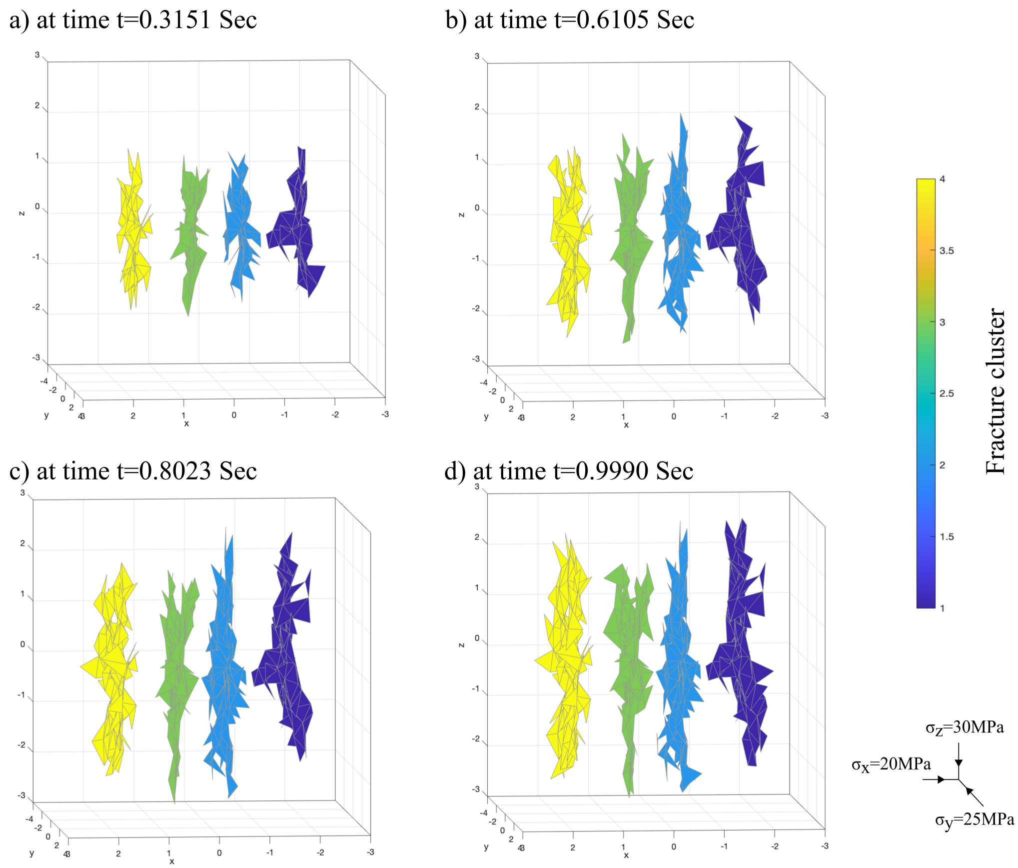

Figure 2-12 Fracture growth of 4 simultaneous injections, side view of the fracture planes is shown here, a) to d) demonstrate adjacent fracture interaction hinders fracture height growth as injection continues.

2.6. Limitations and future work

This work investigated the complexity caused by in-situ stress contrast and the stress disturbance between adjacent hydraulic fractures. Besides these two factors, pre-existing discontinuity in the rock also plays a dominant role in fracture complexity. For future work, natural fractures and bedding planes could be incorporated in the simulation to study the complex geometry generated.

Although a relatively arbitrary fracture trajectory is allowed to develop thanks to the unstructured mesh adopted by FDEM, a mesh sensitivity study could be conducted to quantitively measure the effect of mesh size on the fracture complexity.

2.7. Conclusion

A numerical simulation of the hydraulic fracturing process is conducted using the 3-D hybrid finite-discrete element method. The fracture initiation and propagation are explicitly modeled by implementing the concept of non-linear fracture mechanics using cohesive crack elements. The complexity of the fracture geometry is evident in terms of heterogeneity and anisotropy of the permeability of local cracks. In order to analyze the complexity of the fracture geometry, a method to calculate the local permeability is proposed based on "cubic law" using the aperture of the flow channel.

Chapter 3
Fracture geometry in a reservoir simulator

3.1. Problem description

Hydraulic fracturing technology has been widely applied over the past few decades to maximize the production of unconventional reservoirs with low permeability. The mature horizontal drilling techniques prompt the development of multi-stage hydraulic fracturing allowing for stimulating the same producing pad more efficiently.

Prior to the actual fracturing treatment, numerical simulation of the treatment can provide a prediction on the reservoir response to different injection schemes, allowing for optimization on the treatment design. As is observed both in field cases and laboratory experiments, a few factors play crucial roles affecting the production enhancement, such as the complexity of the fracture network created by the injection. With the capability of the flow simulator CMG, the reservoir response to the different fracture network generated can be studied.

CMG IMEX is a reservoir simulator that can forecast flow behavior during reservoir activities such as production, water flooding, hydraulic fracturing, or other reservoir treatments. It employs an implicit finite difference time integration scheme to calculate reservoir pressure and temperature, allowing for larger time step size to save the computation cost.

The reservoir rock mass is mostly simulated by models constructed with rectangular grid block mesh, in Cartesian or orthogonal corner point grid notation, where the users can specify the size of the grid block to achieve desired resolution for simulating different sizes of reservoir field. Worth noting is the feature of a logarithmically-spaced, locally-refined grid block where reservoir properties like permeability can be assigned to a small fraction of the block instead of the whole grid block. The reservoir field can be simulated by relatively large parent grid blocks to save computation time while still preserve the detail of the heterogeneity in the rock mass.

Due to the limitations of the fracture mechanics module in CMG, the common practice is to take the fractured rock mass as an input geometry from a third-party geomechanics simulator. The network is recognized as a fracture by the significant permeability value assigned to the fractured grid blocks compared to the surrounding grid blocks, which represent the intact rock matrix.

Below is a brief summary of the existing methods available for importing fracture geometry into the CMG reservoir grid.

3.2. Directly define bi-wing fracture plane

3.2.1. Workflow

A simple bi-wing planar fracture is defined in the pre-existing reservoir grid this way. A universal fracture width is assigned, which determines the permeability of this fracture throughout the entire fracture plane with no variation along the fracture height and half-length. Examples of the planar fractures are shown in Figure 3-1.

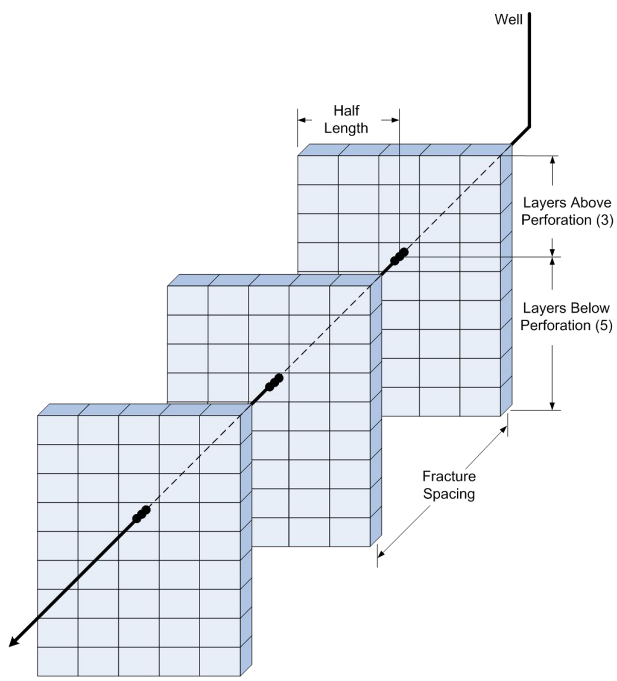

Figure 3-1 Bi-wing, planar fracture imported into CMG.

A logarithmic, locally refined fracture grid is commonly employed by CMG to represent the fracture channel in the rock mass. In order to have a larger parent grid block size to save computation time, a smaller fracture channel can be placed inside the parent block, which is divided into several refined grid blocks. The width of the refined grid block is determined using

$$K_{effective} = \frac{w_{fracture} \times K_{intrinsic}}{w_{block}} \tag{13}$$

Where $K_{effective}$ is the effective permeability used in the inner refined grid hydraulic fracture block by the simulator, W_{block} is the inner fracture block width, which is universal throughout the fracture plane, $K_{intrinsic}$ is the intrinsic permeability determined by the imported fracture geometry from the third party geo-mechanical simulator, and $W_{fracture}$ is the intrinsic width of the fracture, which is the actual aperture of the fracture channel.

3.2.2. Capabilities

This fracture network definition enables the generation of a simple, planar fracture with a universal fracture width and homogenous permeability throughout the whole plane at different half-length and fracture height.

This feature also allows the model to define more than one fracture plane with different properties hence multi-stages fractures along one well.

3.2.3. Limitations

With the universally assigned fracture width within each fracture stage, this fracture model in presented is not able to capture the heterogeneity of the complex fracture geometry, resulting in unrealistic fluid flow calculation, therefore potentially sabotaging the numerical simulation for post-treatment production.

3.3. Import fracture geometry using templates

Fracture permeability data can be readily exported to excel sheets from third-party geo-mechanical simulators, and then this data can be imported into CMG using the permeability template.

3.3.1. Workflow

The fracture geometry can be defined by assigning conductivity values calculated from fracture width at different location of the fracture. Different conductivity values at different height along the half-length can be entered. Refinements are applied with logarithmic spacing so that the blocks get progressively larger when going from the inner fracture block out towards the non-fractured block.

The conductivity values are calculated for the fracture channel at different locations using the intrinsic fracture width and permeability. Then a nominal fracture block width is defined by the user based on the level of refinement desired to reduce the size of the fracture channel. The nominal fracture block width is calculated as in equation (13) individually.

3.3.2. Capabilities

This model allows fracture width variation along the half-length and height of the fracture plane; In this way, heterogeneous permeability can be specified at different locations in the fracture geometry, as shown in **Figure 3-2**.

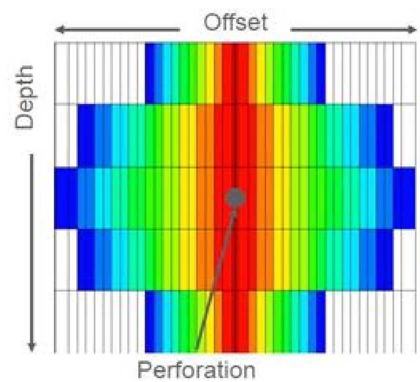

Figure 3-2 Permeability at different fracture length and height.

3.3.3. Limitations

The geometry is still a bi-wing planar model where the half-length does not vary at different fracture height. The permeability assigned in fractured grid blocks is assumed as isotropic, with the simplification of the plane of fracture to be completely vertical. This simplification does not take into account the deviation of the direction of the fracture plane developed under complex in-situ stress conditions.

The imported fracture geometry inherently has a coarse resolution as it is limited by the mesh size of the third party geo-mechanical simulator.

3.4. Import fracture geometry from micro-seismic data

Micro-seismic data can be obtained from acoustic emission data in laboratory HF experiments, actual field micro-seismic monitoring data, or from geo-mechanical simulator simulating HF.

3.4.1. Workflow

Using the location of the micro-seismic events recorded as fracture location (as shown in Figure 3-3), the event location can be imported through the built-in template feature then a reservoir grid can be built depending on the reservoir size and the resolution needed.

Fracture width is input by the user, calculated as effective fracture width, uniform throughout the entire fracture geometry, as shown in Figure 3-4.

3.4.2. Capabilities

This model allows the imported fracture geometry to partially demonstrate the heterogeneity feature of the permeability property in the complex fracture network due to the complex geometry.

It can capture exactly the location of each fracture, with varying fracture height along the half-length of the fracture. Therefore, it presents the fracture as a complex network in the reservoir grid, showing the irregular geometry compared to the simple bi-wing planar fracture model.

3.4.3. Limitations

One is not allowed to specify the aperture or fracture width at different location of the fracture, nor take into account the event energy of each seismic event. As a result, the fracture defined has a uniform fracture width, and therefore a uniform permeability instead of capturing the diminishing aperture towards the fracture tip. The intrinsic anisotropy feature is also not captured as all the fractures portraited are facing one direction.

Moreover, the resolution of the grid block employed in the simulation cannot match the simulation requirement if the frequency of the micro-seismic events occurring becomes too high.

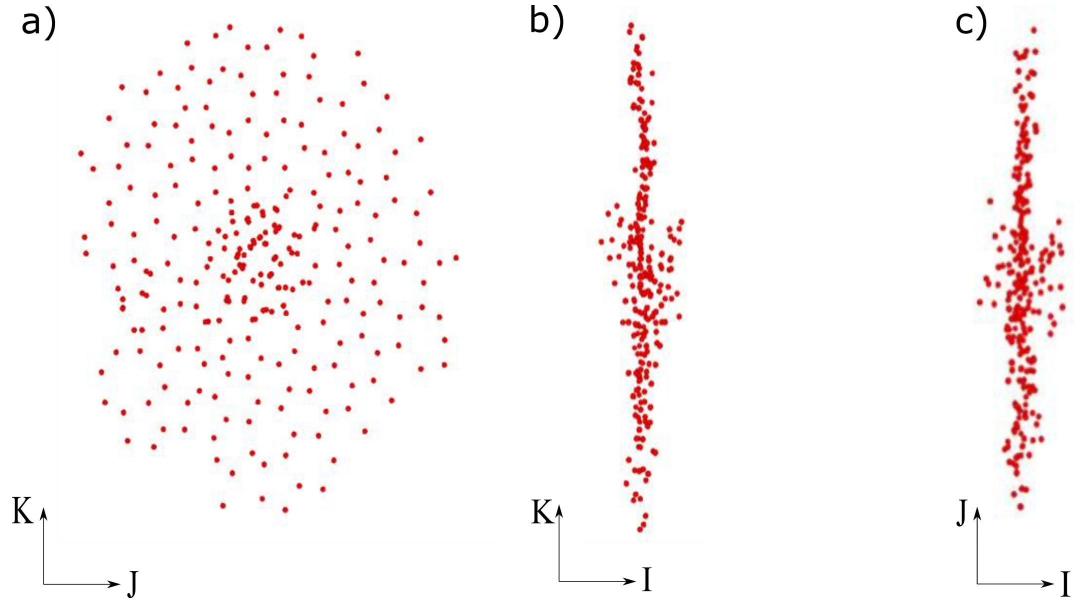

Figure 3-3 Micro-seismic event location in 2-D view, a) axis JK view; b) axis IK view; c) axis IJ views.

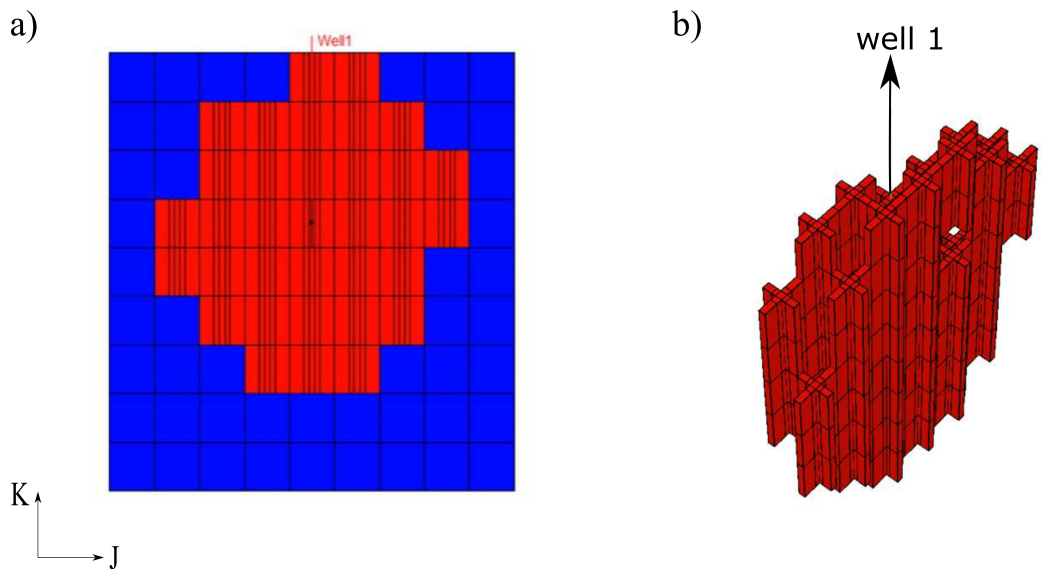

Figure 3-4 Fracture network represented in CMG reservoir grid blocks based on micro-seismic event location. a) 2-D, J-K axis view; b) 3-D view with the arrow annotating wellbore trajectory.

3.5. Summary

This chapter presented existing methods for defining the fracture geometry for the reservoir that has been hydraulic-fractured prior to conducting flow calculations to assess the treatment in the reservoir simulator. The geometry of fracture is defined by manually inputting the fracture width, height, or by defining the permeability of the fracture generated through other third-party geo-mechanical simulators. In this way, reservoir production simulation can be performed in order to assess the hydraulic fracturing treatment designed and simulated in geo-mechanical simulators. However, all the existing methods addressed above fail to fully capture the complexity of the fracture geometry as summarized in Table 3-1. While in Chapter 2, the complexity of the fracture was demonstrated as the heterogeneity and anisotropy of one characteristic attribute – permeability of the fracture simulated through the proposed FDEM method. This calls for a method that can better convey the complexity of the fracture geometry from the geo-mechanical simulator into the reservoir simulator, which is proposed in the next chapter.

Table 3-1 Summary of the existing methods to define fracture geometry in the reservoir simulator CMG.

Method	Source of the fracture geometry	Heterogeneity	Anisotropy
3.2. Directly define bi-wing fracture plane	Manually defined by the user	Fails to capture the heterogeneity of the fracture	Fails to capture the anisotropy of the fracture
3.3. Import fracture geometry using templates3.2. Directly define bi-wing fracture plane	Third-party geo-mechanical simulator	Inherits the heterogeneity of the fracture	Fails to capture any anisotropy of the fracture.
3.4. Import fracture geometry from micro-seismic data	Third-party geo-mechanical simulator Irazu	Inherits the heterogeneity of the fracture	Fails to fully-capture the anisotropy of the fracture.

Chapter 4
Workflow to import the complex fracture geometry into the reservoir simulator

This chapter provides a detailed description of the workflow to import the complex fracture geometry from the geo-mechanical simulator into the reservoir simulator. The hydraulic fracturing simulation example is described earlier in Chapter 2.

4.1. Model setup for the FDEM simulation

4.1.1. Rock properties, strength, boundary conditions

As demonstrated in Chapter 2, a hydraulic fracturing treatment in a shale reservoir is simulated as injecting water into the rock with the geo-mechanical properties of the rock as listed in Table 4-1.

Table 4-1 Mechanical properties of the reservoir rock.

Property (unit)	Value
Density, ρ (kg/m^3)	2500
Young's modulus, E (GPa)	30
Poisson's ratio, ν (-)	0.2
Internal friction coefficient, μ_i (-)	0.6
Internal cohesion, c (MPa)	20
Intrinsic tensile strength, f_t (MPa)	5
Mode I fracture energy, G_{Ic} (J/m^2)	10
Mode II fracture energy, G_{IIc} (J/m^2)	100

The reservoir has the following in-situ properties as listed in **Table 4-2**.

Table 4-2 Initial in-situ reservoir properties.

Properties	Value
Initial in-situ horizontal major principal stress σ_{xx} (MPa)	20
Initial in-situ horizontal minor principal stress σ_{yy} (MPa)	25
Initial in-situ vertical stress σ_{zz} (MPa)	30
Initial fluid pressure in the reservoir (Pa)	0

The fluid injection is simulated under the following operating scheme as listed in Table 4-3.

Table 4-3 Operating parameters for hydraulic fracturing.

Operating parameters	Value
Fluid injection rate (kg/s)	0.5
Shut-in time (Seconds)	1

4.1.2. Description of the fracture generated in Irazu

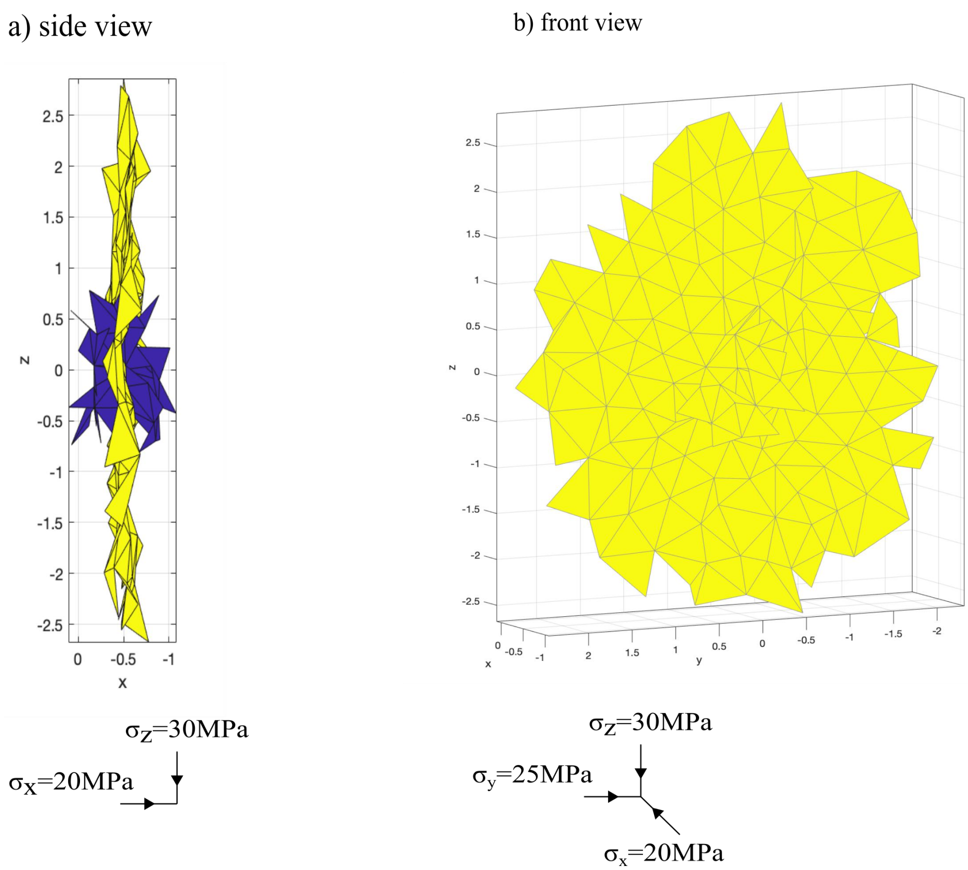

Figure 4-1 a) side view and b) front view of fracture consisting of connected BCCEs (Broken cohesive crack elements) serving as flow channels. The complexity near the injection point is colored in blue in a) for effect.

4.2. Step breakdown of the workflow

As discussed in Chapter 3, for the fracture simulated through the FDEM method, the fracture is not completely planar and therefore, the permeability of the fracture network inherits heterogeneity and anisotropy. In order to convey the realistic complex fracture network from the geomechanical simulator to the reservoir simulator CMG, a workflow is proposed below for this procedure.

<table>
<tr><th>Steps</th><th>Step goal</th><th>Step breakdown</th></tr>
<tr><td>Step 1</td><td>Export the crack element coordinates</td><td>

Take the center of every 6-noded CCE

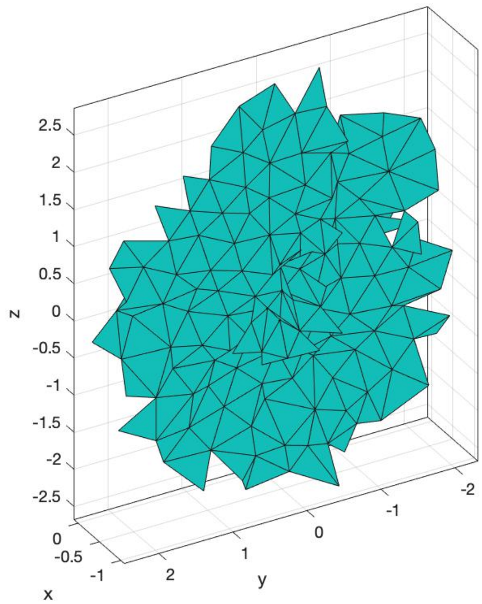

Figure 4-2 Connected flow channels.

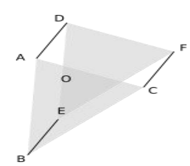

Figure 4-3 Single flow channel.

The coordinate of the centre O is calculated by taking the average of the coordinates of the six nodes:

$$O(x,y,z) = \frac{A(x,y,z)+B(x,y,z)+C(x,y,z)+D(x,y,z)+E(x,y,z)+F(x,y,z)}{6} \qquad (14)$$

</td></tr>
<tr><td>Step 2</td><td>Calculate local fracture (represented by each crack element)</td><td>Each permeability vector has magnitude and direction, as discussed in Chapter 3. Each crack element (flow channel) is considered to have one characteristic direction, which is represented by the normal vector of the crack element plane, as shown below in Figure 4-4 as the flow is only allowed in the flow channel plane, which is</td></tr>
</table>

Steps	**Step goal**	**Step breakdown**
	orientation	perpendicular to the normal vector. 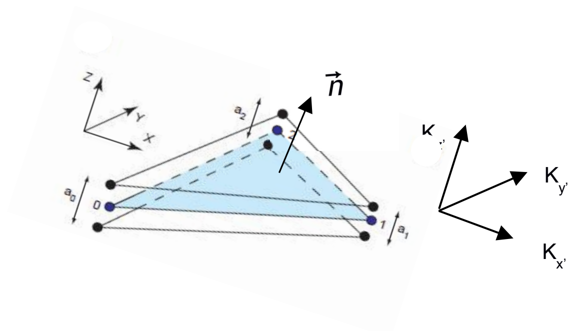 **Figure 4-4** Direction of the crack element (flow channel) represented by its normal vector. The absolute value of the permeability is the magnitude (length) of the vector.
Step 3	Calculate absolute permeability in the flow channel, for every CCE (cohesive crack element) in the fracture process zone.	Each crack element is regarded as a flow channel, as shown in Figure 4-4. Considering the classic parallel plate fracture model, "cubic" law can be applied: $$K = \frac{a^2}{12} \quad (15)$$ Where *a* is the aperture/opening of the crack element (flow channel). In this way, the permeability is represented using an absolute value associated with that crack element by the crack element coordinates.
Step 4	Resolve permeability into all three directions along the principal coordinate axes, so that permeability can be represented as a tensor, i.e., three components	In order to manipulate the permeability of every CCE for future reservoir fluid flow simulation in the global cartesian coordinates, the direction of the permeability has to be defined in the global coordinates. Since the flow is only restricted in the direction perpendicular to the plane of the flow channel, which can be represented by the normal vector to the crack element plane. The permeability tensor can be projected onto the global cartesian axes by subtracting the component in the direction of the normal vector from the component

<table>
<tr><th>Steps</th><th>Step goal</th><th>Step breakdown</th></tr>
<tr><td></td><td>perpendicular to each other along the principal axes. This allows the entire modeled fractured reservoir rock to have permeability values at three directions, representing a realistic, complex fracture network instead of a simplified planar fracture.</td><td>in the direction of the base vector of that crack element as described in equation (12) below
$$\vec{K} = [K_x \quad K_y \quad K_z] = K \times [1 \quad 1 \quad 1] - K \times \vec{n} \qquad (16)$$
Where $\vec{K}$ is the desired permeability tensor, K is the absolute value(magnitude) of the permeability of the flow channel as calculated above in equation (15) for every crack element, [1 1 1] is the base vector and $\vec{n}$ is the normal vector in global coordinates, as shown on below illustration Figure 4-5.
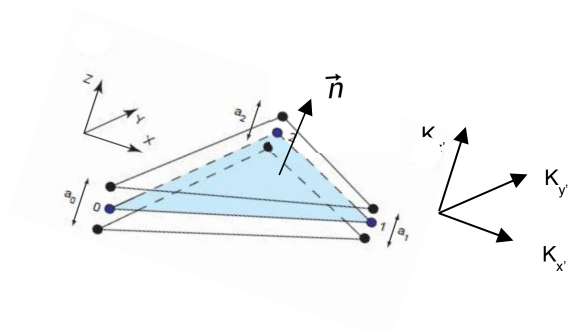

Figure 4-5 Permeability calculation for each crack element.
Now, the permeability tensor is expressed in terms of global coordinates for every crack element. In this way it can be determined how much flow is allowed in the x, y, and z-direction, respectively.</td></tr>
<tr><td>Step 5</td><td>To import the fracture network geometry into the CMG grid block</td><td>Map the permeability tensor at each flow channel (crack element) to the CMG grid block.
Each CMG grid block is correlated with one or more crack elements (flow channel) from Irazu depending on the resolution of the mesh in CMG.
Since the permeability of each grid block in CMG can have three directions: I, J, and K correlated with the x, y, and z-direction in Irazu. The permeability tensor can be assigned in three directions, respectively, as shown in the permeability tensor of each grid in I, J, and K directions. The permeability in the I direction is the smallest,</td></tr>
</table>

Steps	Step goal	Step breakdown
		which is reasonable as the fracture plane is perpendicular to the I-axis corresponding to the minimum in-situ stress.
Step 6	Initiate reservoir grid in CMG	Calculate how many reservoir parent grid blocks are needed to match the size of the reservoir modeled in Irazu.
Step 7	Import permeability in the three orthogonal directions in terms of the grid block	Initiate a matrix used as a tally to locate fractured blocks based on non-zero permeability values. Import the prepared matrix containing permeability values in three directions of every grid block that has been identified as a fractured grid block based on previous codes.
Step 8		Change the color scale representing the permeability in CMG to logarithmic scale, as shown in Figure 4-6. 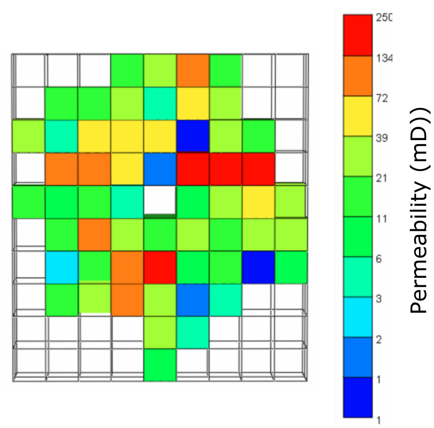 **Figure 4-6** Permeability (mD) for flow along the I axis assigned to each grid block.

Steps	Step goal	Step breakdown
		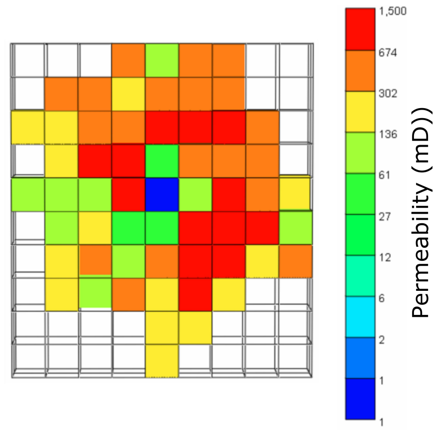 **Figure 4-7** Permeability (mD) for flow along J axis assigned to each grid block. 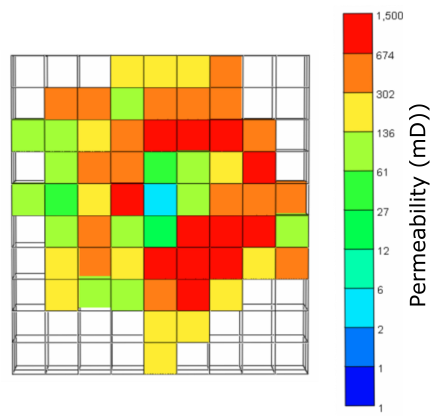 **Figure 4-8** Permeability (mD) for flow along K axis assigned to each grid block.
Step 9		When adjusting the scaling the mesh, if multiple crack elements fall within one CMG grid block, the crack element with the largest aperture (therefore largest permeability) was assigned to the CMG grid block.
Step 10	Expand the reservoir grid, so that multiple stages of fractures	Upon establishing the desired resolution of the grid block size, the reservoir field to be simulated can be expanded to include more stages of fracturing treatments.

Steps	Step goal	Step breakdown
	can be imported into CMG simultaneously for future simulation.	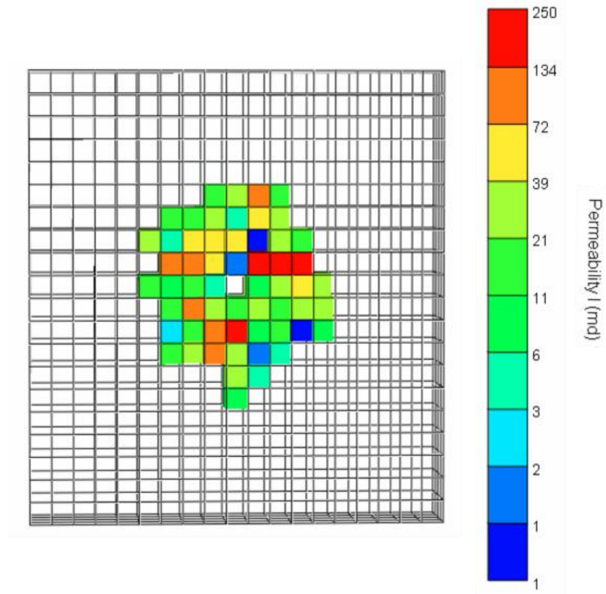 **Figure 4-9** Permeability (mD) for flow along I axis assigned to each grid block in the expanded reservoir grid.
Step 11	Assign permeability to the refined fracture channel	CMG mesh geometry has the advantage that it can partition a parent grid block into smaller sub-grid blocks. The permeability can be assigned to a sub grid block instead of the parent grid block. In this way, the parent grid block can have a larger size (resolution is determined by the size of the reservoir field needed to simulate), with realistic conductivity values and smaller fracture widths, while using less parent grid block to save computation time. The sub-grid blocks can be divided logarithmically, gradually reducing the block size to the desired fracture width. Grid refinement is needed around fractures to capture the transient flow with the least amount of total grid blocks.

Steps	Step goal	Step breakdown
Step 12	Import geometry from multi-stage hydraulic fracturing	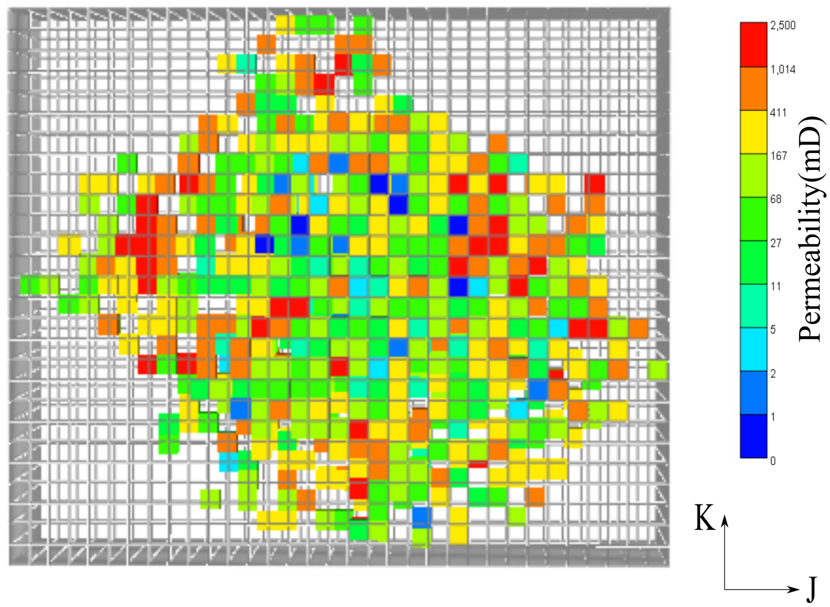 **Figure 4-10** Permeability (mD) for flow along I direction of the reservoir after four stages of hydraulic fracturing, JK-axis view. 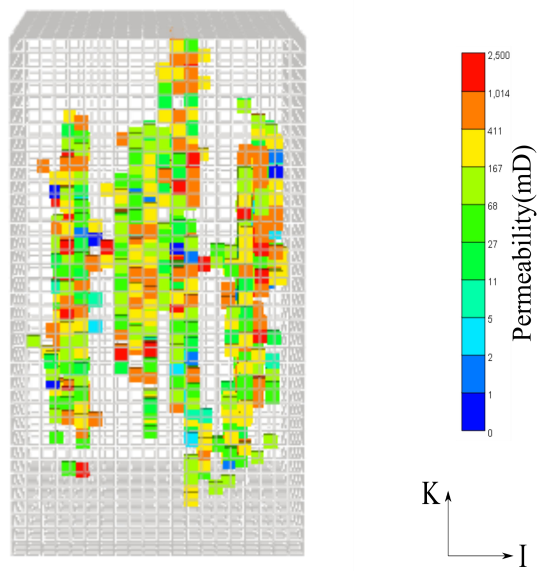 **Figure 4-11** Permeability (mD) for flow along I direction of the reservoir after four stages of hydraulic fracturing, IK-axis view.

4.3. Discussion

4.3.1. Complex fracture geometry capture

As demonstrated in Chapter 2, the hybrid finite-element methods excel among various techniques modeling the hydraulic fracturing process in that it can capture the complexity of the fracture geometry. The complexity of the fracture geometry is illustrated as the heterogeneity and the anisotropy of the local permeability tensor on the fracture. The permeability is resolved into three orthogonal directions along the three axes in the reservoir grid, respectively. Finally, this complex fracture geometry is captured in the reservoir simulator CMG, as shown in Figure 4-12 and Figure 4-13.

Compared to the conventional fracture geometry representations as listed in Table 3-1, this workflow allows the hydraulic fracturing treatment design to be assessed more accurately through numerical modeling.

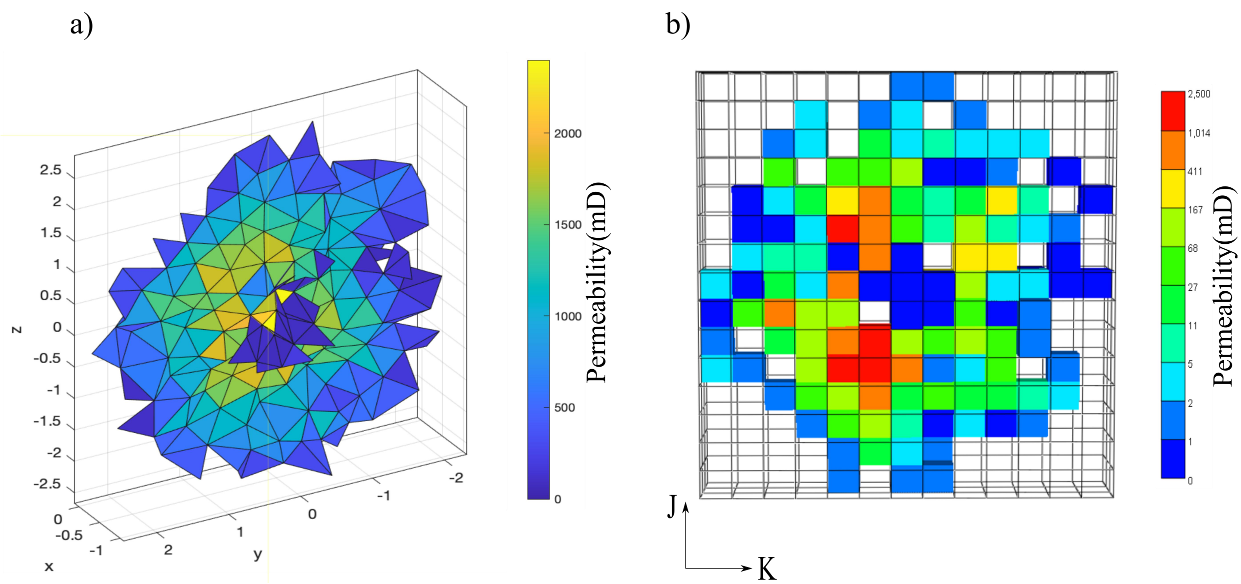

Figure 4-12 Absolute value of permeability in each flow channel captured in a) FDEM and b) CMG grid blocks.

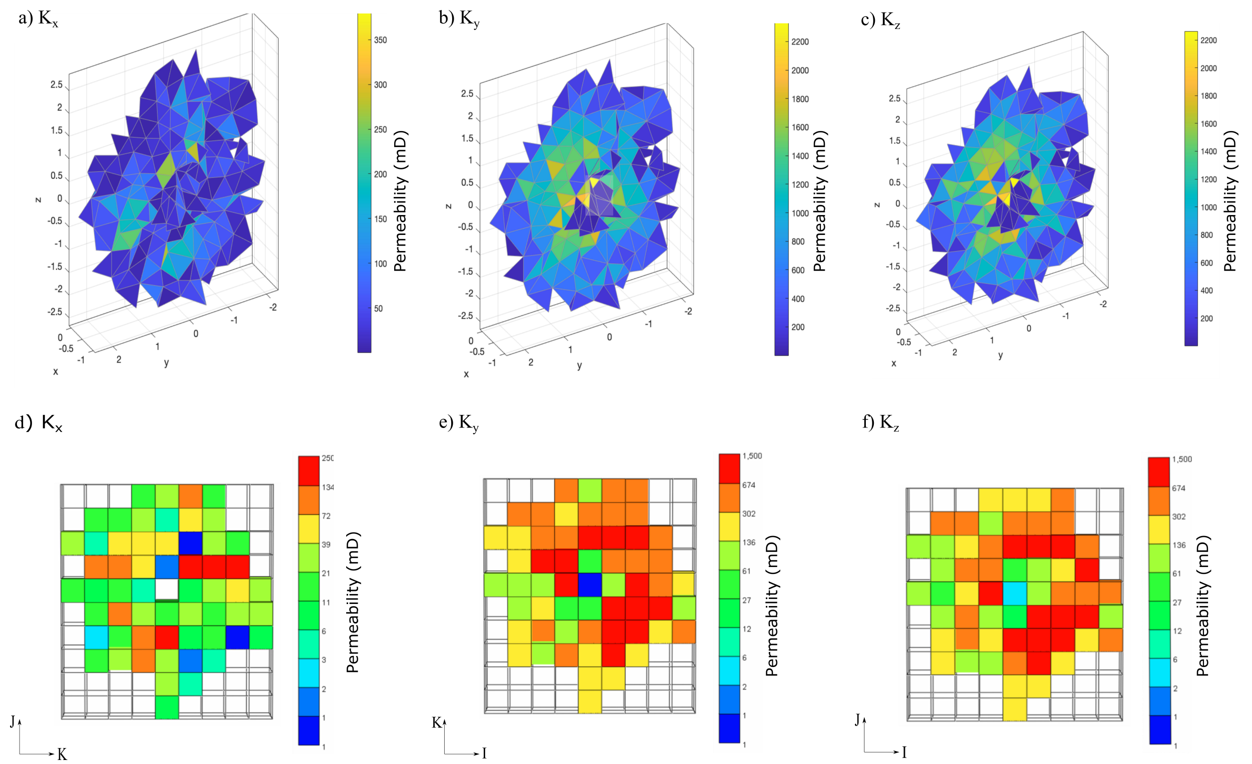

Figure 4-13 Permeability tensor resolved to global x, y, and z-axis, represented in the flow channels in Irazu Vs. grid blocks in CMG.

As shown in Figure 4-12, the fracture geometry exported from Irazu (taken from the example hydraulic fracturing in Chapter 2 can be mapped to grid blocks in CMG. Although some details at the edge of the fracture geometry are not perfectly captured, the permeability is captured to a more refined resolution reflecting the spatial variation in the aperture of the fracture.

Anisotropy of permeability is captured, as shown in Figure 4-13, the flow is more restricted in the x-direction with a much smaller permeability than the y and z-direction.

4.3.2. Production simulation

In order to further demonstrate the necessity of capturing the complex fracture geometry, reservoir production is modeled in CMG based on the fracture geometry above and the simple bi-wing planar fracture. Reservoir properties are assumed for common shale gas formation with a pore pressure of 9000 psi and 400 nD permeability.

A specific gas production rate is specified in the simulation in order to mimic the mechanical choke restriction in actual production where the production rate is restricted by the choke size, instead of the reservoir capacity. The resulting gas production rate and bottom hole pressure are compared for the two fracture geometries, as in Figure 4-14.

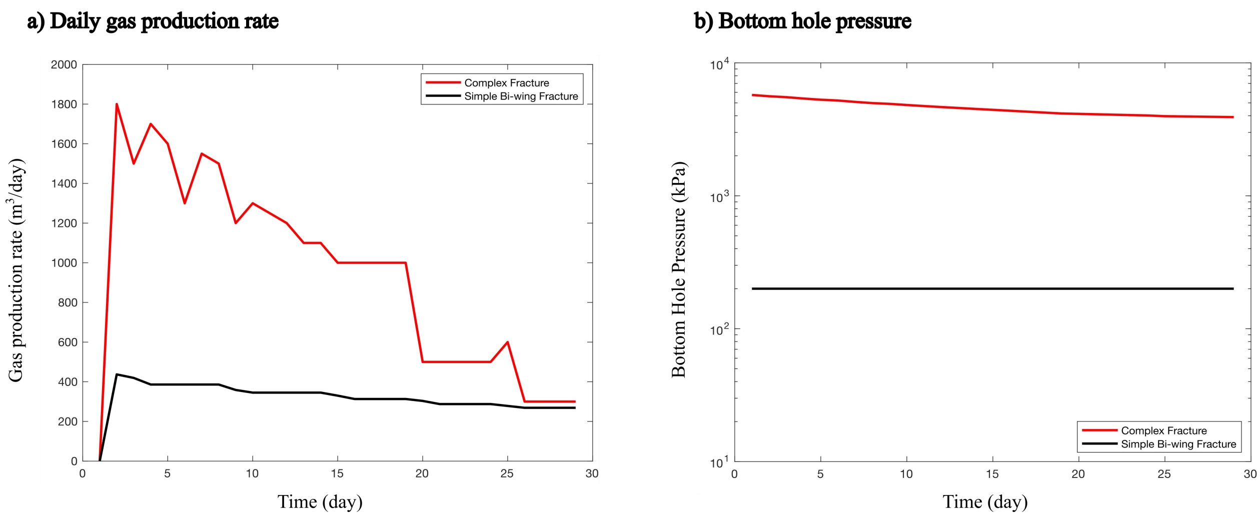

Figure 4-14 a) Surface gas production rate; b) Well bottom hole pressure.

Both surface gas production rate and bottom hole pressure drawdown of the simple bi-wing fracture are lower than the complex fracture case. Evidently, the EUR (estimated ultimate recovery) for the bi-wing fracture model would also be lower than the complex fracture model. This result conforms to the field observation that it is the complexity of fracture that correlates with EUR instead of fluid volume pumped or fracture half-length (Fisher et al., 2004). The higher production could be explained by the fact that more surface area and SRV (stimulated reservoir volume) are generated using the complex fracture model. This correlation between the larger surface area created by the complex fracture with the enhance in production could be further studied.

4.3.3. Limitations

The tetrahedral mesh in the FDEM geo-mechanical simulator is random and non-orthogonal, whereas in the reservoir fluid flow simulator CMG, the grid is orthogonal. The positions of the crack elements cannot be perfectly mapped to the grid blocks in the reservoir simulator CMG. A more robust calibration workflow is needed for a more realistic representation of the reservoir.

Only 30 days of producing is modelled, demonstrating the difference between complex and simple fracture geometry in the initial post-treatment period. However, the production of the reservoir with complex fracture might decline faster and a longer producing life should be modelled to study the long-time reservoir performance with simple and complex fracture.

The boundary pressures for the reservoir model are set fixed over the producing life, which do not account for the far-field pressure effect.

The hydraulic fractures created would have larger porosity than the matrix porosity. Oil and gas would be produced from the fracture to the wellbore first and then from the matrix to the fracture. A dual-porosity model could be adopted to account for this effect.

4.4. Future work

4.4.1. Mechanical earth model

In reservoir exploitation and other field operations it is beneficial to have an accurate numerical model of the reservoir, the concept of mechanical earth model (MEM) (Ahmed et al., 2014; Al-Zubaidi & Al-Neeamy, 2020; Knöll, 2016; Plumb et al., 2000) is widely adapted to the industry. Starting from the geologic structural model and incorporating the in-situ stress and rock geomechanical properties, a consolidated mechanical earth model can provide better understanding of the reservoir. Among the properties identified in the mechanical earth model, in-situ stress state and rock mechanical properties such as Young's modulus and Poisson's ratio are of particular interests to conduct geomechanical analysis for drilling and reservoir treatment designs. The mechanical earth model can be built based on field seismic and logging data while using laboratory core testing data and single-well pressure testing data as calibration to the model.

Conventionally, the mechanical earth model is built by collecting and analyzing core, log, seismic, and field pressure testing data (Suarez-Rivera et al., 2013). Recently, micro-seismic monitoring during HF treatments also provides valuable information on many mechanical properties and in-situ stress conditions contributing to the MEM. However, since the accuracy of micro-seismic data is limited by many factors, the interpretations of the data can be controversial and not definitive.

The proposed workflow provides another innovative way to probe some of the reservoir properties by utilizing the readily available production data after HF treatments. It is essentially a robust "history-matching" process by coupling the FDEM and CMG simulator.

4.4.2. Interpretation of field pressure tests

The fluid injection process studied above also occurs in other situations such as field pressure tests aiming at interpreting the in-situ stress state of the reservoir.

Diagnostic fracture injection test (DFIT) and several flow-back testing schemes are common practice to calibrate the stress state.

However, anomalies have been observed in the field pressure testing curves using the conventional DFIT interpretation methods (Zheng et al., 2020). These pressure tests have the same mechanism as hydraulic fracturing in the rock mass. The existing analytical and numerical methods to interpret the pressure testing curves assume simple planar fracture and homogeneous reservoir, which turns out problematic for neglecting the heterogeneity and anisotropy of the rock properties in the MEM. Therefore, the anomalies observed in the field pressure testing curves caused by the complex rock mass could be studied using the workflow proposed above.

A DFIT simulation using the FDEM simulator (without consideration of the multi-phase reservoir fluid flow calculation in the reservoir simulator) can be performed (as shown in Figure 4-15) and serve as a reference to calibrate input rock mass properties.

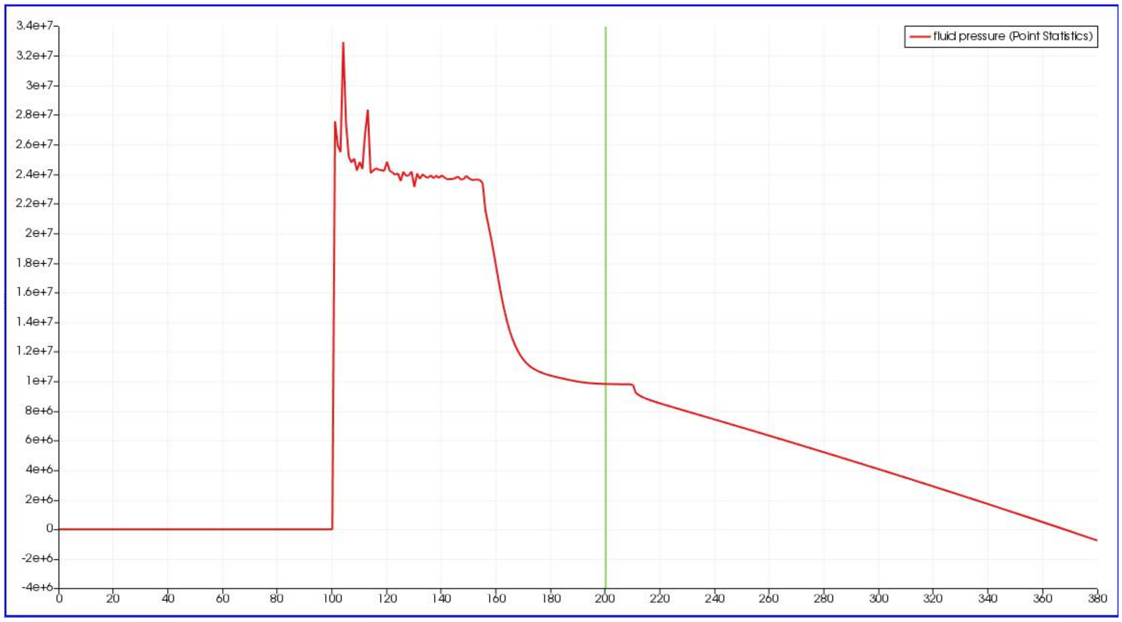

Figure 4-15 Simulation of a "DFIT", σ_1=20MPa, σ_2=25MPa, σ_3=30MPa, with initial reservoir pressure P_o = 6MPa, fluid pressure is shown at the injection point.

Chapter 5
Conclusion and future work

5.1. Conclusion

Upon briefly reviewing the history of modeling the process of hydraulic fracturing, the capacities and limitations of these analytical and numerical modeling techniques are summarized. Among the fully-discretized numerical simulation techniques, the hybrid finite-discrete element method (FDEM) combining the merits of the continuum and discontinuum-based modeling techniques. In this research, the 3-D FDEM method implemented by the commercial software Irazu is adopted to simulate the hydraulic fracturing process for its ability to explicitly describing the fracture. The continuum-based finite element mesh employed by FDEM allows accurate capturing of the elastic deformation of the rock under loading. Due to the non-linear fracture mechanics concept adopted for the cohesive crack elements after exceeding the peak strength of the finite elements, fracture initiation and propagation process can be explicitly modeled. A fluid solver is fully coupled to the mechanical solver by using the cohesive crack elements as the fluid flow channel and converting the fluid pressure to nodal force on the finite elements.

The fracture geometry is analyzed by plotting the broken cohesive elements. Variation in the direction of the fracture plane is shown locally as the normal vector to each cohesive crack element. A novel approach is proposed to calculate the local permeability based on the concept of "cubic law" using the aperture and the direction of each cohesive crack element. The complexity of the fracture geometry is demonstrated by capturing the heterogeneity and anisotropy of the permeability tensor.

In order to assess the hydraulic treatment design by running production forecasting using the reservoir simulator CMG, the complex fracture geometry needs to be imported from the geo-mechanical simulator Irazu into the reservoir simulator CMG. However, there is no existing method to import the complex fracture geometry into CMG. Utilizing the local permeability tensor calculation method proposed, a workflow is further laid out to map the permeability tensor obtained from the commercial FDEM simulator Irazu to the reservoir grid block in the reservoir simulator CMG. The complex fracture geometry can then be captured by the reservoir grid block in CMG.

A demonstrative production simulation is conducted in CMG comparing the simple bi-wing planar fracture geometry and the complex fracture generated in Irazu. The distinct difference in gas production and pressure drawdown between the two fracture geometries indicate the effect of fracture geometry on production.

5.2. Limitation and future work

This work serves as a starting point to realize the coupling between the geo-mechanical simulator and reservoir simulator to aid with the design of hydraulic fracturing treatment. A few recommendations can be made from this research.

The workflow proposed is merely a one-way coupling mapping the fracture geometry from the FDEM geo-mechanical simulator to the reservoir simulator. Future production simulation would benefit from a more integrated method to achieve full coupling with the ability to feed the fluid pressure back to the geo-mechanical simulator and update the fracture geometry during production simulation.

The micro-mechanical rock properties input into the FDEM simulator are inferred from the calibration process based on macro-mechanical laboratory tests where the core samples are obtained from the reservoir sites. Whereas the rock properties could also be inferred from the "history matching process" using the post-treatment production data utilizing this workflow. Alternatively, micro-seismic monitoring data could be used to calibrate the input parameters by matching the location, energy, and mechanism of the fracture events. A monte-carlo simulation could be employed to calculate a possible range of the resulting fracture geometry and production based on assigned distribution of the input parameters.

If preliminary field injection data is available, it can be used to calibrate the input rock properties in the geo-mechanical simulator directly by comparing the field data with the injection pressure response simulated using the workflow proposed in this research.

Pre-existing discontinuities in the rock including discrete fracture networks (DFN) and bedding planes could be incorporated into the rock mass to investigate the interactions between the pre-existing fracture and the induced fractures.

References

Abe, H. (1976). Growth Rate of a Penny-Shaped Crack in Hydraulic Fracturing of Rocks. *Journal of Geophysical Research*, *81*(29).

Adachi, J., Siebrits, E., Peirce, A., & Desroches, J. (2007). Computer simulation of hydraulic fractures. *International Journal of Rock Mechanics and Mining Sciences*, *44*(5), 739–757. https://doi.org/10.1016/j.ijrmms.2006.11.006

Advani, S. H., & Lee, J. K. (1982). Finite Element Model Simulations Associated With Hydraulic Fracturing. *Society of Petroleum Engineers Journal*, *22*(02), 209–218. https://doi.org/10.2118/8941-PA

Advani, S. H., Lee, T. S., & Lee, J. K. (1990). Three-Dimensional Modeling of Hydraulic Fractures in Layered Media: Part I—Finite Element Formulations. *Journal of Energy Resources Technology*, *112*(1), 1–9. https://doi.org/10.1115/1.2905706

Ahmed, S., Khan, K., Omini, P., Abdulaziz, A., Ahmed, M., Yadav, A. S., & Mohiuddin, M. A. (2014). An integrated drilling and geomechanics approach helps to successfully drill wells along the minimum horizontal stress direction in khuff reservoirs. *Society of Petroleum Engineers - 30th Abu Dhabi International Petroleum Exhibition and Conference, ADIPEC 2014: Challenges and Opportunities for the Next 30 Years*, *1*, 749–761. https://doi.org/10.2118/171755-ms

Al-Zubaidi, N. S., & Al-Neeamy, A. K. (2020). 3D mechanical earth model for Zubair oilfield in southern Iraq. *Journal of Petroleum Exploration and Production Technology*, *10*(5), 1729–1741. https://doi.org/10.1007/s13202-020-00863-y

Barenblatt, G. I. (1962). *The Mathematical Theory of Equilibrium Cracks in Brittle Fracture* (H. L. Dryden, T. von Kármán, G. Kuerti, F. H. van den Dungen, & L. B. T.-A. in A. M. Howarth (eds.); Vol. 7, pp. 55–129). Elsevier. https://doi.org/https://doi.org/10.1016/S0065-2156(08)70121-2

Britt, L. K., & Smith, M. B. (2009). Horizontal Well Completion, Stimulation Optimization, and Risk Mitigation. In *SPE Eastern Regional Meeting* (p. 17). Society of Petroleum Engineers.

https://doi.org/10.2118/125526-MS

Budyn, É., Zi, G., Moës, N., & Belytschko, T. (2004). A method for multiple crack growth in brittle materials without remeshing. *International Journal for Numerical Methods in Engineering*, *61*(10), 1741–1770. https://doi.org/10.1002/nme.1130

Chen, Z. (2013). *An ABAQUS Implementation of the XFEM for Hydraulic Fracture Problems* (p. Ch. 36). IntechOpen. https://doi.org/10.5772/56287

Cipolla, C. L., Warpinski, N. R., Mayerhofer, M. J., Lolon, E. P., & Vincent, M. C. (2010). The relationship between fracture complexity, reservoir properties, and fracture treatment design. *Society of Petroleum Engineers - SPE Asia Pacific Oil and Gas Conference and Exhibition 2010, APOGCE 2010*, *1*, 44–68. https://doi.org/10.2118/115769-ms

Cramer, D. D. (2008). Stimulating Unconventional Reservoirs: Lessons Learned, Successful Practices, Areas for Improvement. In *SPE Unconventional Reservoirs Conference* (p. 19). Society of Petroleum Engineers. https://doi.org/10.2118/114172-MS

Dahi-Taleghani, A., & Olson, J. E. (2011). Numerical modeling of multistranded-hydraulic-fracture propagation: Accounting for the interaction between induced and natural fractures. *SPE Journal*, *16*(3), 575–581. https://doi.org/10.2118/124884-PA

De Borst, R., Sluys, L. J., Mühlhaus, H. B., & Pamin, J. (1993). Fundamental issues in finite element analyses of localization of deformation. In *Engineering Computations* (Vol. 10, Issue 2, pp. 99–121). https://doi.org/10.1108/eb023897

De Kock, T., Boone, M. A., De Schryver, T., Van Stappen, J., Derluyn, H., Masschaele, B., De Schutter, G., & Cnudde, V. (2015). A Pore-Scale Study of Fracture Dynamics in Rock Using X-ray Micro-CT Under Ambient Freeze–Thaw Cycling. *Environmental Science & Technology*, *49*(5), 2867–2874. https://doi.org/10.1021/es505738d

Dershowitz, W. S., Cottrell, M. G., Lim, D. H., & Doe, T. W. (2010). A Discrete Fracture Network Approach For Evaluation of Hydraulic Fracture Stimulation of Naturally Fractured Reservoirs. In *44th U.S. Rock Mechanics Symposium and 5th U.S.-Canada Rock Mechanics Symposium* (p. 8). American Rock Mechanics Association. https://doi.org/

Du, C. M., Zhang, X., Zhan, L., Gu, H., Hay, B., Tushingham, K., & Ma, Y. Z. (2010). Modeling Hydraulic Fracturing Induced Fracture Networks in Shale Gas Reservoirs as a Dual Porosity System. In *International Oil and Gas Conference and Exhibition in China* (p. 13). Society of Petroleum Engineers. https://doi.org/10.2118/132180-MS

Dugdale, D. S. (1960). Yielding of steel sheets containing slits. *Journal of the Mechanics and Physics of Solids*, *8*(2), 100–104. https://doi.org/https://doi.org/10.1016/0022-5096(60)90013-2

Fan, L., Thompson, J. W., & Robinson, J. R. (2010). *CSUG / SPE 136696 Understanding Gas Production Mechanism and Effectiveness of Well Stimulation in the Haynesville Shale Through Reservoir Simulation*. *June*, 1–15.

Fisher, M. K., Heinze, J. R., Harris, C. D., Davidson, B. M., Wright, C. A., & Dunn, K. P. (2004). Optimizing horizontal completion techniques in the barnett shale using microseismic fracture mapping. *SPE Annual Technical Conference Proceedings*. https://doi.org/10.2118/90051-ms

Fisher, M. K., Wright, C. A., Davidson, B. M., Goodwin, A. K., Fielder, E. O., Buckler, W. S., & Steinsberger, N. P. (2002). Integrating fracture-mapping technologies to improve stimulations in the Barnett shale. *SPE Production and Facilities*, *20*(2), 85–93. https://doi.org/10.2118/77441-PA

Fu, P., Johnson, S. M., & Carrigan, C. R. (2013). An explicitly coupled hydro-geomechanical model for simulating hydraulic fracturing in arbitrary discrete fracture networks. *International Journal for Numerical and Analytical Methods in Geomechanics*, *37*(14), 2278–2300. https://doi.org/10.1002/nag.2135

Fung, R. L., Vilayakumar, S., & Cormack, D. E. (1987). Calculation of Vertical Fracture Containment in Layered Formations. *SPE Formation Evaluation*, *2*(04), 518–522. https://doi.org/10.2118/14707-PA

Geertsma J;, & F, D. K. (1969). Rapid Method of Predicting Width and Extent of Hydraulically Induced Fractures. *J Petroleum Technology*, *21*(12), 1571–1581.

Geomechanica Inc. (2018). *Irazu 3D Geomechanical Simulation Software. Theory Manual*.

Hattori, G., Trevelyan, J., Augarde, C. E., Coombs, W. M., & Aplin, A. C. (2017). Numerical Simulation of Fracking in Shale Rocks: Current State and Future Approaches. *Archives of Computational Methods in Engineering*, *24*(2), 281–317. https://doi.org/10.1007/s11831-016-9169-0

Hillerborg, A., Modéer, M., & Petersson, P.-E. (1976). Analysis of crack formation and crack growth in concrete by means of fracture mechanics and finite elements. *Cement and Concrete Research*, *6*(6), 773–781. https://doi.org/https://doi.org/10.1016/0008-8846(76)90007-7

Ida, Y. (1972). Cohesive force across the tip of a longitudinal-shear crack and Griffith's specific surface energy. *Journal of Geophysical Research (1896-1977)*, *77*(20), 3796–3805. https://doi.org/10.1029/JB077i020p03796

Itasca, U. (1996). Universal distinct element code. *Users Manual*, *1*.

Keshavarzi, R., Mohammadi, S., & Bayesteh, H. (2012). Hydraulic Fracture Propagation In Unconventional Reservoirs: The Role of Natural Fractures. In *46th U.S. Rock Mechanics/Geomechanics Symposium* (p. 8). American Rock Mechanics Association. https://doi.org/

Khristianovic, S. A., & Zheltov, Y. P. (1955). Formation of vertical fractures by means of highly viscous liquid. *World Petroleum Congress Proceedings*, *1955-June*, 579–586.

Knöll, L. (2016). *The Process of Building a Mechanical Earth Model Using Well Data*. https://www.mendeley.com/viewer/?fileId=554d030a-17f3-f285-6c4d-a7d6a5bf7858&documentId=f4b91a59-9423-3f5a-9aea-e623667ae994

Lam, K. Y., Cleary, M. P., & Barr, D. T. (1986). A Complete Three-Dimensional Simulator for Analysis and Design of Hydraulic Fracturing. In *SPE Unconventional Gas Technology Symposium* (p. 11). Society of Petroleum Engineers. https://doi.org/10.2118/15266-MS

Lisjak, A., & Grasselli, G. (2014). A review of discrete modeling techniques for fracturing processes in discontinuous rock masses. *Journal of Rock Mechanics and Geotechnical*

Engineering, *6*(4), 301–314. https://doi.org/https://doi.org/10.1016/j.jrmge.2013.12.007

Lisjak, A., Mahabadi, O. K., Tatone, B. S. A., Alruwaili, K., Couples, G. D., Ma. J., J., & Al-Nakhli, A. (2015). 3D Simulation of Fluid-Pressure-Induced Fracture Nucleation and Growth in Rock Samples. In *American Rock Mechanics Association.* American Rock Mechanics Association.

Lisjak, A., Tatone, B. S. A., Grasselli, G., & Vietor, T. (2014). Numerical modelling of the anisotropic mechanical behaviour of opalinus clay at the laboratory-scale using FEM/DEM. *Rock Mechanics and Rock Engineering*, *47*(1), 187–206. https://doi.org/10.1007/s00603-012-0354-7

Lisjak, A., Tatone, B. S. A., Kaifosh, P., He, L., Mahabadi, O. K., & Grasselli, G. (2016). Development of a fully-coupled, hydro-mechanical model for finite-discrete element simulations of fluid-driven fracturing. *50th US Rock Mechanics / Geomechanics Symposium 2016*, *1*(i), 818–828.

Mahabadi, O. K., Lisjak, A., Munjiza, A. A., & Grasselli, G. (2012). Y-Geo: New combined finite-discrete element numerical code for geomechanical applications. *International Journal of Geomechanics*, *12*(6), 676–688. https://doi.org/10.1061/(ASCE)GM.1943-5622.0000216

Moës, N., Dolbow, J., & Belytschko, T. (1999). A finite element method for crack growth without remeshing. *International Journal for Numerical Methods in Engineering*, *46*(1), 131–150. https://doi.org/10.1002/(SICI)1097-0207(19990910)46:1<131::AID-NME726>3.0.CO;2-J

Munjiza, A. A. (2004). *The combined finite-discrete element method*. John Wiley & Sons.

Munjiza, A. A., Owen, D. R. J., & Bicanic, N. (1995). A combined finite-discrete element method in transient dynamics of fracturing solids. *Engineering Computations*, *12*(2), 145–174. https://doi.org/10.1108/02644409510799532

Nagel, N., Zhang, F., Sanchez-Nagel, M., Lee, B., & Agharazi, A. (2013). Stress shadow evaluations for completion design in unconventional plays. *Society of Petroleum Engineers*

- *SPE Canadian Unconventional Resources Conference 2013 - Unconventional Becoming Conventional: Lessons Learned and New Innovations*, *1*(November), 120–133. https://doi.org/10.2118/167128-ms

Nordgren, R. P. (1972). Propagation of a Vertical Hydraulic Fracture. *Society of Petroleum Engineers Journal*, *12*(04), 306–314. https://doi.org/10.2118/3009-PA

Perkins, T. K., & Kern, L. R. (1961). Widths of Hydraulic Fractures. *Journal of Petroleum Technology*, *13*(09), 937–949. https://doi.org/10.2118/89-PA

Plumb, R., Edwards, S., Pidcock, G., Lee, D., & Stacey, B. (2000). The mechanical earth model concept and its application to high-risk well construction projects. *IADC/SPE Drilling Conference*.

Potyondy, D. O. (2012). PFC 2D flat joint contact model. *Itasca Consulting Group Inc, Minneapolis*.

Pyrack-Nolte, L. J., Myer, L. R., Cook, N. G. W., & Witherspoon, P. A. (1987). *Hydraulic and mechanical properties of natural fractures in low-permeability rock*. https://www.osti.gov/biblio/6406367

Ramandi, H. L., Armstrong, R. T., & Mostaghimi, P. (2016). Micro-CT image calibration to improve fracture aperture measurement. *Case Studies in Nondestructive Testing and Evaluation*, *6*, 4–13. https://doi.org/10.1016/j.csndt.2016.03.001

Reynolds, O. (1886). IV. On the theory of lubrication and its application to Mr. Beauchamp tower's experiments, including an experimental determination of the viscosity of olive oil. *Philosophical Transactions of the Royal Society of London*, *177*, 157–234.

Rogers, S. F., Elmo, D., & Dershowitz, W. S. (2011). Understanding Hydraulic Fracture Geometry And Interactions In Pre-Conditioning Through DFN And Numerical Modeling. In *45th U.S. Rock Mechanics / Geomechanics Symposium* (p. 6). American Rock Mechanics Association. https://doi.org/

Settari, A., & Cleary, M. P. (1986). Development and Testing of a Pseudo-Three-Dimensional Model of Hydraulic Fracture Geometry. *SPE Production Engineering*, *1*(06), 449–466.

https://doi.org/10.2118/10505-PA

Siebrits, E., & Peirce, A. P. (2002). An efficient multi-layer planar 3D fracture growth algorithm using a fixed mesh approach. *International Journal for Numerical Methods in Engineering*, *53*(3), 691–717. https://doi.org/10.1002/nme.308

Simonson, E. R., Abou-Sayed, A. S., & Clifton, R. J. (1978). Containment of Massive Hydraulic Fractures. *Society of Petroleum Engineers Journal*, *18*(01), 27–32. https://doi.org/10.2118/6089-PA

Sneddon, I. N. (1946). The distribution of stress in the neighbourhood of a crack in an elastic solid. *Proceedings of the Royal Society of London. Series A. Mathematical and Physical Sciences*, *187*(1009), 229–260. https://doi.org/10.1098/rspa.1946.0077

Sousa, J. L., Carter, B. J., & Ingraffea, A. R. (1993). Numerical simulation of 3D hydraulic fracture using Newtonian and power-law fluids. *International Journal of Rock Mechanics and Mining Sciences And*, *30*(7), 1265–1271. https://doi.org/10.1016/0148-9062(93)90106-N

Stokes, G. G. (1905). *reprinted in: Mathematical and Physical Papers, vol. 5*. Cambridge University Press, Cambridge.

Suarez-rivera, R., Herring, S., Oil, E., Handwerger, D., Marino, S., Petriello, J., Stevens, K., Oil, E., & Company, O. (2013). *SPE 167204 Integrated Analysis of Core Geology , Rock Properties , Well Logs , and Seismic Data Provides a Well Constrained Geologic Model of the Bossier / Haynesville System*.

Tatone, B. S. A., & Grasselli, G. (2015). A calibration procedure for two-dimensional laboratory-scale hybrid finite-discrete element simulations. *International Journal of Rock Mechanics and Mining Sciences*, *75*, 56–72. https://doi.org/10.1016/j.ijrmms.2015.01.011

Vandamme, L., & Curran, J. H. (1989). A three-dimensional hydraulic fracturing simulator. *International Journal for Numerical Methods in Engineering*, *28*(4), 909–927. https://doi.org/10.1002/nme.1620280413

Warpinski, N. R., & Branagan, P. T. (1989). Altered-Stress Fracturing. *Journal of Petroleum*

Technology, *41*(09), 990–997. https://doi.org/10.2118/17533-PA

Warpinski, N. R., Kramm, R. C., Heinze, J. R., & Waltman, C. K. (2005). Comparison of single- and dual-array microseismic mapping techniques in the barnett shale. *Proceedings - SPE Annual Technical Conference and Exhibition*, 913–922.

Warpinski, N. R., Mayerhofer, M. J., Vincent, M. C., Cipolla, C. L., & Lolon, E. R. (2009). Stimulating unconventional reservoirs: Maximizing network growth while optimizing fracture conductivity. *Journal of Canadian Petroleum Technology*, *48*(10), 39–51. https://doi.org/10.2118/114173-PA

Warpinski, N. R., & Teufel, L. W. (1987). Influence of Geologic Discontinuities on Hydraulic Fracture Propagation (includes associated papers 17011 and 17074). *Journal of Petroleum Technology*, *39*(02), 209–220. https://doi.org/10.2118/13224-PA

Wu, K. (2014). Numerical modeling of thermal fracture development in unconventional reservoirs. *PhD Dissertation*. http://hdl.handle.net/2152/28050

Zheng, S., Manchanda, R., Wang, H. Y., & Sharma, M. (2020). DFIT analysis and interpretation in layered rocks. *Society of Petroleum Engineers - SPE Hydraulic Fracturing Technology Conference and Exhibition 2020, HFTC 2020*, 4–6. https://doi.org/10.2118/199690-ms

Zimmerman, R. W., & Bodvarsson, G. S. (1994). *Hydraulic conductivity of rock fractures*.